Politecnico di Torino

ScuDo
Scuola di Dottorato ~ Doctoral School
WHAT YOU ARE, TAKES YOU FAR

Doctoral Dissertation
Doctoral Program in Physics (36^{th}cycle)

Design, fabrication, and characterization of optical and photonic metasurfaces

By

Vittorio Bonino

******

Supervisor(s):
Prof. F.C. Pirri, Supervisor
Dr. A. Angelini, Co-Supervisor

Doctoral Examination Committee:
Prof. L. Mino, Referee, Università degli Studi di Torino
Dr. A. Tomasino, Referee, École Polytechnique Fédérale de Lausanne

Politecnico di Torino
2024

Declaration

I hereby declare that, the contents and organization of this dissertation constitute my own original work and does not compromise in any way the rights of third parties, including those relating to the security of personal data.

Vittorio Bonino
2024

* This dissertation is presented in partial fulfillment of the requirements for **Ph.D. degree** in the Graduate School of Politecnico di Torino (ScuDo).

Acknowledgements

I would like to express my profound gratitude to my co-supervisor, Dr. Angelo Angelini, who has been a pivotal support throughout my doctoral journey. He was able to transmit to me not only important notions but also the passion for the field. I would like to acknowledge Prof. Fabrizio Pirri and the Polytechnic University of Turin for providing me the opportunity to pursue this PhD. Similarly, I wish to extend my thanks to Prof. Cristina Benea for the opportunity to spend a significant period at EPFL, where I was able to develop a significant and crucial part of my thesis. I offer my appreciation to all my colleagues in Italy and Switzerland who generously shared their expertise and played an essential role in the accomplishments presented in this thesis. Last, but certainly not least, I am eternally thankful to my family for their unwavering support at every stage of my studies.

Abstract

This doctoral thesis provides a comprehensive exploration of optical and photonic metasurfaces, emphasizing their design, fabrication, and characterization. It delves into the innovative realm of manipulating light at the nanoscale through metasurfaces, a transformative approach that offers a versatile platform for tailoring electromagnetic wave behavior. The research encompasses a rigorous analysis of metalenses, large area metasurfaces, resonances in nanopillar structures, and organic metasurfaces contributing significantly to the field by addressing gaps in current understanding and presenting novel material characterization methods, systemic design techniques, and advanced fabrication strategies. Through this work, the thesis aims to enhance the knowledge and application of metasurface technologies, offering new perspectives for future technological developments in photonics and optical technologies.

Contents

Introduction

In the realm of modern optics and photonics, the manipulation of light at the nanoscale has emerged as a pivotal research area, paving the way for groundbreaking technological advancements with profound implications across various domains. This doctoral thesis embarks upon an exhaustive exploration of metasurfaces, a field that represents a paradigm shift in the way we control and harness light.

The central argument of this thesis revolves around metasurfaces, with a specific focus on their design, fabrication, and characterization for photonics applications. Metasurfaces are two-dimensional arrays of subwavelength-scale nanostructures that are engineered to manipulate the properties of light in unprecedented ways. This transformative technology offers a versatile platform for tailoring the behavior of electromagnetic waves, encompassing a wide spectrum of applications from imaging and sensing to telecommunications and beyond.

Metasurfaces represent a disruptive departure from traditional optical components. Conventional optical systems, often reliant on bulky and complex arrangements of lenses and mirrors, have inherent limitations in terms of size, weight, and aberrations. Metasurfaces, in contrast, offer ultrathin, planar optical elements that can be engineered with remarkable precision to manipulate light in unconventional ways. The fundamental concept underlying metasurfaces is the precise tailoring of the electromagnetic response of their constituent nanostructures, allowing for unprecedented control over the amplitude, phase, and polarization of light.

While metasurfaces have achieved remarkable successes, they are not without challenges and unanswered questions. There is a continual quest to deepen our fundamental understanding of metasurface behavior, including complex phenomena such as optical resonances, dispersion engineering, and nonlinearity.

The optimization of fabrication techniques for metasurfaces, including lithographic methods, self-assembly, and nanoimprinting, is a critical area of research. Achieving scalability and cost-effectiveness while maintaining precision is an ongoing challenge. The choice of materials for metasurface design is a crucial consideration. Integrating metasurfaces with other optical components and systems, as well as exploring novel material platforms, is a subject of intense investigation.

This doctoral thesis takes a comprehensive approach to explore the multifaceted dimensions of metasurface research, encompassing four substantial chapters.

First of all, we will embark on a thorough Literature Review, delving into the historical development, fundamental principles, and key breakthroughs in the field of metasurfaces. Subsequently we will deepen the methodologies employed in this research, offering insights into design principles, fabrication techniques, and characterization methods specifically tailored for metasurfaces. It will provide the foundational framework upon which subsequent chapters are built.

Chapter 1 brings the focus to Metalenses, unraveling their design intricacies, fabrication processes, and characterization for beam focusing applications. We illustrate how metasurfaces can revolutionize traditional optical systems, particularly lenses.

Chapter 2 ventures into the realm of Large Area Metasurfaces, exploring the scalability and practicality of these metasurfaces. We address the challenges and opportunities associated with large area metasurface fabrication and their broad-ranging applications.

Chapter 3 investigates Resonant Nanopillar Metasurfaces, unveiling their spectral properties, fabrication intricacies, and potential applications. We delve into the world of resonant nanostructures, showcasing their significance in the metasurface arena.

Chapter 4 concludes the journey by exploring the integration of Organic Polymers as a versatile material platform for metasurfaces. We explore the unique properties of organic polymers and their potential applications within the metasurface landscape.

Together, these chapters offer insights, innovations, and empirical findings that collectively advance the field of photonics and optical technologies, contributing to the broader scientific community's understanding and appreciation of this transformative research area.

Literature review

The concept of metasurfaces has been discussed in the literature for over twenty years. The initial efforts to manipulate the optical properties of 2D surfaces date back to 2000, as evidenced by references [1] and [2]. Consequently, it took more than a decade to witness the emergence of first concepts of creating sub-wavelength nanostructures. These would eventually be termed meta-atoms, designed to manipulate light phase and intensity, thereby creating surfaces with customized optical properties. This advancement was made possible through the development of more advanced nanofabrication techniques [3, 4].

The enormous advantages of this new technology has been evident immediately and progressive and extended theoretical research has been developed uninterrupted for the following years both on the structuring of sub-wavelength films [5, 6] and on theoretical models [7, 8].

In parallel to the development of theoretical research, there has also been a significant advancement in fabrication processes. These advancements have enabled greater control over light properties [9] and improvements in performance [10].

With this grow prospective is not surprising to see in how many field metasurfaces established a relevant presence, specially in the field of optics and photonic where metasurfaces are largely used in lenses and imaging [11, 12], holography [13, 14], beam steering and shaping [15, 16], and polarization control [17, 18].

This thesis seeks to offer in-depth analysis and studies of the phenomena involved in metasurface technologies. This is to enhance the knowledge and awareness of the underlying principles governing the functioning of metasurfaces. Through this research, we endeavour to bridge the gap between theoretical knowledge and practical application, thereby advancing the field and offering new perspectives for future technological developments.

Theoretical Hints

To fully understand the topics covered in this thesis, it might be essential to clarify some theoretical concepts underlying the operation of metasurfaces. Metasurfaces for optic applications obviously involve the interaction of light with the materials composing the metasurface. Thus, a brief overview of light-matter interaction is crucial. Maxwell's equations are pivotal in this area, as they describe how light propagates through materials and lay the groundwork for understanding the optical properties of materials.

0.1 Maxwell's equations

Maxwell's equations are a collection and a generalization of four fundamentals electromagnetic laws:

Gauss's Law for Electricity ($\nabla \bullet E = \frac{\rho}{\varepsilon_0}$) states that electric fields diverge from electric charges. In matter, this means electric fields are influenced by the presence of charged particles.

Gauss's Law for Magnetism ($\nabla \bullet B = 0$) indicates there are no "magnetic charges". Instead, magnetic fields form closed loops, and this is relevant in materials with magnetic properties.

Faraday's Law of Induction ($\nabla \times E = -\frac{\partial B}{\partial t}$) shows that a changing magnetic field creates an electric field. This is key in understanding how electromagnetic waves (like light) propagate.

Ampère's Law with Maxwell's Addition ($\nabla \times B = \mu_0 J + \mu_0 \varepsilon_0 \frac{\partial E}{\partial t}$) reveals how electric currents and changing electric fields produce magnetic fields. This is crucial in materials where currents are induced by electromagnetic radiation.

In the particular case when there are no charges or currents present the solution to Maxwell's Equations describe light as an electromagnetic wave, with electric and magnetic fields oscillating perpendicular to each other and to the direction of propagation.

On the other hand, when light encounters matter, its electric field interacts with the electrons in atoms or molecules. This can cause electrons to move, absorbing energy from the light (absorption), or electrons can release energy back as light (emission or scattering).

In dielectric materials, the electric field in light induces dipole moments by displacing the charges, which is the basis for the material's polarization. The response of the material, described by its permittivity, affects how the light wave propagates through it.

At interfaces, changes in material properties, like permittivity and permeability, lead to partial reflection and refraction of light. The frequency dependence of material responses, like permittivity, leads to dispersion (light changing speed and bending) and absorption (loss of light energy within the material).

0.2 Permittivity

Electric permittivity is a measure of the ability of a material to allow the formation of an electric field within it. It essentially describes how an electric field affects, and is affected by a dielectric medium. When an electric field is applied to a material, it causes the electric charges within the material to slightly shift from their equilibrium positions. This displacement results in the alignment of microscopic dipoles within the material, a process known as polarization. The permittivity of the material determines the degree to which these dipoles align in response to the field. In the context of Maxwell's Equations, permittivity appears in the relationship between the electric displacement field (D) and the electric field (E), given by

$$D = \varepsilon E \tag{1}$$

This equation shows how an electric field induces an electric displacement or polarization in a medium.

0.3 Polarizability

When an external electric field (E) interacts with an atom or molecule, it can displace the negatively charged electrons with respect to the positively charged nucleus, creating an induced dipole moment (p). The induced dipole moment (p) in a material is proportional to the applied electric field (E). This relationship is defined as $p = \alpha E$, where α is the polarizability of the atom or molecule. Polarizability measures how easily the electron cloud in an atom or molecule can be distorted by an electric field. Maxwell's Equations, particularly Gauss's Law for Electricity, involve the electric field (E) and the electric displacement field (D). In materials, D is related not only to E but also to the polarization density (P), which is the dipole moment per unit volume. The relationship is given by:

$$D = \varepsilon_0 E + P \tag{2}$$

0.4 Susceptibility

The polarization density (P) of a material is related to the electric field (E) by the electric susceptibility (χ_e) of the material:

$$P = \varepsilon_0 \chi_e E \tag{3}$$

Electric susceptibility is a measure of how much a material will become polarized in response to an applied electric field. In Maxwell's Equations, specifically in the equation for the electric displacement field (D), substituting P from the above equation gives:

$$D = \varepsilon_0 E + \varepsilon_0 \chi_e E \tag{4}$$

This can be simplified to:

$$D = \varepsilon_0 (1 + \chi_e) E \tag{5}$$

Where $\varepsilon_0(1+\chi_e)$ is the permittivity of the material. The permittivity (ε) of a material is thus related to its susceptibility. This relationship shows how the electric susceptibility determines how the electric field propagates through the material.

0.5 Magnetic Permeability

Magnetic permeability (μ) is a measure of how a material responds to and influences a magnetic field. It relates the magnetic field intensity (H) to the magnetic flux density (B):

$$B = \mu H \tag{6}$$

0.6 Metasurfaces physical properties

The macroscopic electromagnetic behaviour of materials and metamaterials, including characteristics like transparency and reflectivity, can be, therefore, fundamentally explained through their electric permittivity (ε) and magnetic permeability (μ). These two parameters play a crucial role in determining how electromagnetic waves, including visible light, interact with a material. Metamaterials can be engineered to have specific ε and μ values that result in unique properties. Some metamaterials are designed to have negative values of ε and μ at certain frequencies [19]. This can lead to negative refraction, where light bends in the opposite direction compared to normal materials. Materials engineered to have ε and μ near zero can slow down light dramatically, leading to enhanced light-matter interactions [20]. This can be used for applications in sensing and switching. By engineering ε and μ appropriately, some metamaterials can absorb all incident light, leading to applications in solar energy harvesting and stealth technology [21].

To achieve such control over electromagnetic properties, metasurfaces exploit meta-atoms. Meta-atoms are subwavelength-scale structures disposed in large arrays that allow a local manipulation of the physical properties of the metasurface. Each meta-atom is designed with specific geometrical features (such as shape, size, and orientation) that determine its electromagnetic response. This design determines how the meta-atom interacts with the electric and magnetic components of light. The arrangement and structure of the meta-atoms can be tailored to create localized regions with specific values of ε and μ. This local modification alters the way electromagnetic waves propagate through or are reflected from these regions. For instance, meta-atoms can be designed to resonate at particular frequencies, enhancing the local electromagnetic response and effectively modifying ε and μ at those frequencies.

Methodology

This section aims to elucidate the methodologies employed to achieve the results presented in the thesis. It provides an overview of the primary methods utilized for the design, fabrication and characterization.

0.7 Design

Finite Element Method (FEM) simulations are a numerical approach used to approximate solutions to partial differential equations (PDEs) that describe various physical phenomena in real-world systems. The foundation of FEM simulations is the division of the computational domain into finite elements. In two dimensions, these elements are often triangles or quadrilaterals, while in three dimensions, they can be tetrahedra or hexahedra. Each element approximates the behavior of the physical field within its boundaries. At the nodes of each finite element, known values or boundary conditions are specified. Interpolation functions, usually polynomials, are employed to approximate the behavior of the field variable within an element based on the values at its nodes.

In this PhD thesis, we employ the powerful computational tool COMSOL Multiphysics®, integrated with its Radio Frequency (RF) module, to conduct FEM simulations in the frequency domain for the comprehensive investigation of metasurfaces' electromagnetic behaviour. Metasurfaces have garnered immense interest in recent years due to their unique ability to manipulate electromagnetic waves at subwavelength scales. Through rigorous numerical simulations, we aim to gain a deeper understanding of the intricate interactions between incident electromagnetic radiation and metasurfaces, thereby elucidating the underlying physical mechanisms that govern their performance. The COMSOL RF module serves as an important

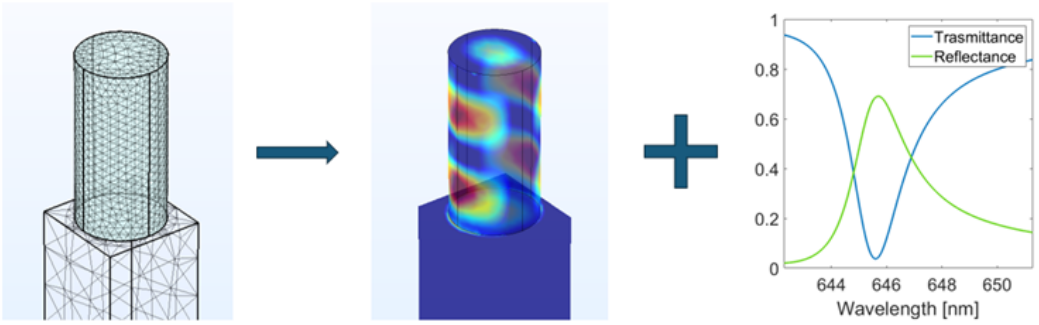

Fig. 1 Schematic overview of the simulation flow. The computation performed on a decomposed domain provides insights into the field distribution within the nanostructure and the overall behavior of the metasurface.

resource, enabling us to model and analyse metasurface structures while considering the frequency-dependency of the materials' complex refractive index. We investigated periodic structures and evaluated the transmission, reflection, and absorption intensity. The metasurface structures consisted of dielectric elements arranged periodically on a glass substrate in an air environment. The materials for the dielectric elements were carefully defined using optical and electric properties obtained from experimental measurements or from existing literature, ensuring accurate representation of their behaviour in the electromagnetic domain.

To assess the transmission properties, a two-port analysis was employed. One port was located at the top surface of the metasurface, while the other was positioned at the bottom surface. The choice of two ports facilitated the characterization of how the metasurface influenced the propagation of electromagnetic waves through it.

Furthermore, the study delved into the generation of confined modes within the metasurface structures using electromagnetic multipole theory for multipole expansion. This theoretical framework allowed for the decomposition of the electromagnetic field into its constituent multipole moments, shedding light on the various modes supported by the periodic arrangement of dielectric elements.

0.8 Fabrication

0.8.1 Electron Beam Lithography

Electron beam lithography (EBL) is a sophisticated technique used to create extremely fine patterns required for fabricating micro- and nanoscale structures and devices. This method is essential in fields such as nanotechnology and advanced material science. In this section, we will explore the principles, instrumentation, and operation of EBL in detail.

EBL systems employ electron sources that generate high-energy electrons. The most common electron sources are based on field emission, which includes cold cathodes or thermionic sources. These sources emit electrons when subjected to an electric field, providing a continuous supply of high-energy electrons. The emitted electrons are then manipulated and focused using a combination of electromagnetic lenses and deflectors. These components are crucial for shaping and directing the electron beam with precision. Electromagnetic lenses use magnetic fields to bend and focus the electron trajectories, ensuring accurate positioning of the beam on the substrate. EBL relies on specialized resist materials that exhibit sensitivity to electron beam exposure. These resists come in two primary categories: positive and negative. Positive resists become more soluble upon electron exposure, while negative resists become less soluble. The choice of resist depends on the desired pattern and application.

The energy of the electrons in the beam is carefully controlled to interact with the resist material in a controlled manner. Depending on the specific resist used and the desired outcome, electron energies typically range from a few keV to several tens of keV. Additionally, the dosage, defined as the number of electrons per unit area, is precisely controlled to achieve the desired pattern resolution and quality. To expose the resist the electron beam is directed onto the substrate. It is scanned across the substrate according to the defined pattern, with the intensity and position carefully controlled. The electron beam interacts with the resist material, inducing changes based on the resist's sensitivity. After exposure, the substrate undergoes a development process. In positive resists, the exposed regions become more soluble and are removed during development, revealing the desired pattern. In negative

resists, the unexposed regions are dissolved away. The development step transforms the exposed pattern into a physical relief structure on the substrate.

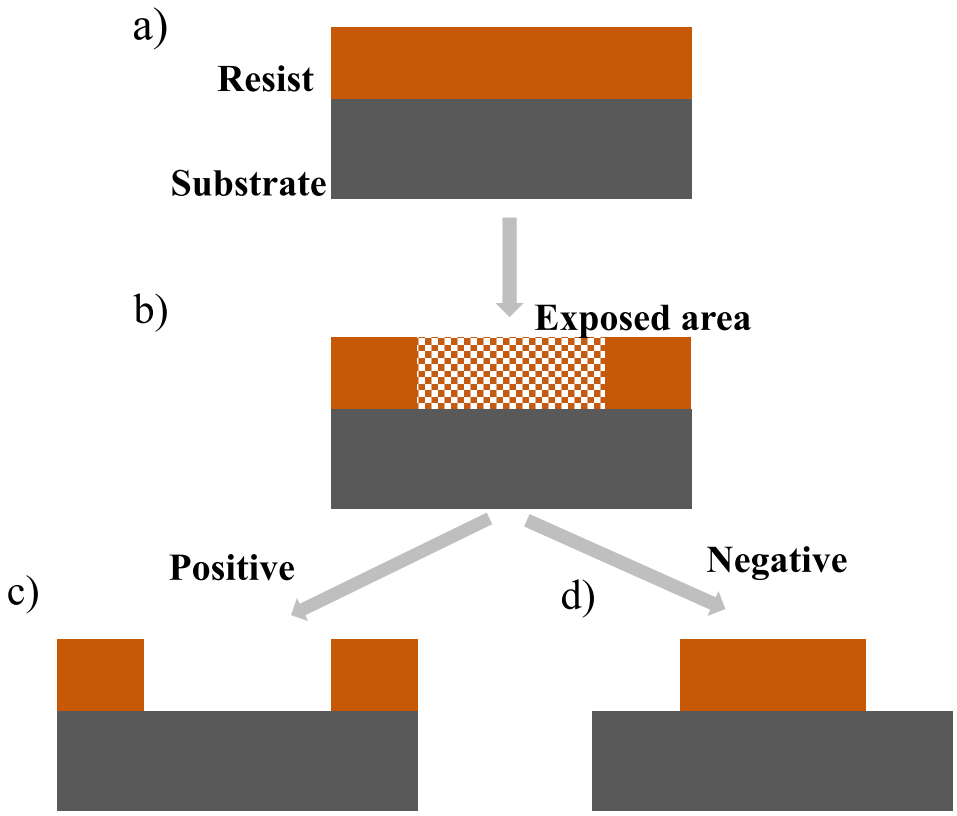

Fig. 2 Scheme of electron beam lithography process flow. **(a)** The electronic resist is spin coated on the substrate. **(b)** Resist is exposed by electron beam, which alters its solubility. In the case of positive resist **(c)**, the exposed area is removed during development. For negative resist **(d)**, the unexposed area is removed, leaving the exposed material intact.

In this work, both negative and positive photoresists were utilized, depending on the required pattern types. For the fabrication of nanopillars, which are diminutive nanostructures, negative photoresists proved to be more advantageous due to their ability to minimize the exposed area. This reduction not only decreases the lithography time required but also mitigates the proximity effect. Specifically, the photoresist ma-N 2401 was chosen for its superior resolution. The photoresist was applied to the sample surface by spin-coating at a speed of 3000 revolutions per minute (rpm) for 30 seconds, resulting in a uniform layer approximately 100 nm thick. Following this, the photoresist layer was exposed to an electron beam with

a dose of 80 $\mu C/cm^2$. For the development of the exposed photoresist, the sample was immersed in a specialized developer solution, ma-D 331, which is comprised of sodium hydroxide.

For larger structures, such as PEDOT optical modulator, consisting of large electric pads, it is more practical to expose the surrounding area. Consequently, a positive photoresist is favored for these applications. Specifically, polymethyl methacrylate (PMMA) 950K A4 was employed. This photoresist forms a thicker layer of approximately 300 nm and necessitates a higher exposure dose of 900 $\mu C/cm^2$.

0.8.2 ICP-CVD

Inductive Coupled Plasma Chemical Vapor Deposition (ICP-CVD) is a sophisticated and versatile thin film deposition technique that plays a pivotal role in semiconductor manufacturing, materials science research, and various industrial applications. This technique enables precise control over the growth of thin films with atomic-level accuracy. ICP-CVD combines the principles of plasma generation, chemical reactions in the gas phase, and controlled substrate heating to deposit high-quality thin films.

The heart of ICP-CVD is the inductive coupled plasma source. This source uses radiofrequency (RF) power to generate a high-energy, ionized plasma from a precursor gas. The RF power creates an oscillating magnetic field, which induces an electrical current in the gas, ultimately leading to the formation of the plasma. The plasma generated in ICP-CVD is typically in the RF range, with electron temperatures ranging from several thousand to tens of thousands of degrees Celsius. This high-energy plasma contains a mix of ions, electrons, radicals, and neutral species. The high-energy plasma environment promotes chemical reactions in the gas phase. These reactions lead to the dissociation and ionization of the precursor gas, forming reactive species that will eventually contribute to the growth of the thin film on the substrate.

Various species of gases were utilized depending on the type of material to be grown. For the growth of hydrogenated amorphous silicon (a-Si:H), silane (SiH_4) was used as the precursor gas. An ICP power of 500 W and a substrate temperature of 250°C were set to initiate the pyrolysis of silane: $SiH_4 \rightarrow Si + 2H_2$. The decomposed

silicon atoms are then adsorbed by the surface, initiating nucleation and subsequent film growth.

For the growth of silicon nitride (SiN), a similar process occurred, with the addition of a precursor gas: ammonia (NH_3). From the ammonia, nitrogen atoms are incorporated into the forming SiN molecule on the surface. For SiN deposition, a higher ICP power of 1500 W was employed, while the substrate temperature remained constant at 250°C.

0.8.3 Reactive Ion Ethcing

Reactive Ion Etching (RIE) is a fundamental microfabrication technique that offers precise control over material removal at the atomic level. RIE relies on a combination of chemical reactions and physical processes to remove material selectively from a substrate. These processes are governed by several fundamental principles, including plasma generation, ion bombardment, and etch selectivity. The heart of RIE is the generation of reactive plasma. This plasma is typically created by applying radiofrequency (RF) power to a gas mixture inside a vacuum chamber. The gas mixture contains the desired etchant gases, such as fluorine-based compounds, which will react with the substrate material. Within the plasma, positively charged ions are accelerated towards the substrate by the electric field. The energy of these ions can be controlled by adjusting the RF power and bias voltage applied to the substrate stage. Importantly, RIE is anisotropic, meaning that the ions bombard the substrate surface at controlled angles, resulting in directional etching. RIE offers the ability to selectively etch one material over another. The selectivity is determined by the difference in etch rates between the materials and can be tailored by choosing the appropriate etchant gases and process conditions.

The pseudo-Bosch process was employed for the selective etching of a-Si and SiN. This method involves alternating between etching and passivation cycles, resulting in highly anisotropic profiles with smooth sidewalls. A gas mixture comprising 50% sulfur hexafluoride (SF_6) and 50% octafluorocyclobutane (C_4F_8) was utilized at a pressure of 10 $mTorr$, with an inductively coupled plasma (ICP) power of 1200 W and a radio frequency (RF) power of 20 W. The substrate temperature was maintained at 10°C.

0.9 Characterization

0.9.1 Ellipsometry

Ellispometry is a powerful technique able to investigate the optical properties and thickness of a material. In Ellipsometry a linearly polarized light is used as probe that makes it to reflect on the sample surface at different angles. A detector collects the reflected light and a measure of the change in polarization is performed.

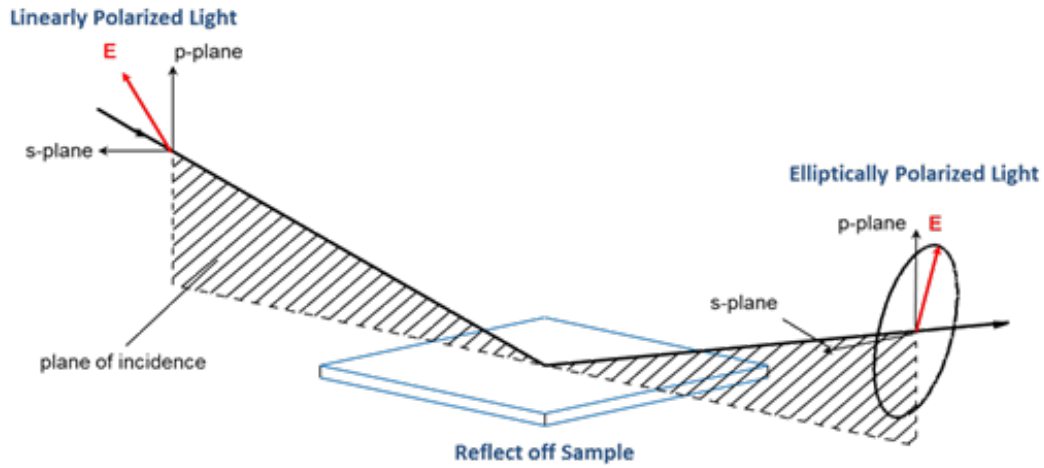

Fig. 3 Diagram illustrating the setup for an ellipsometry measurement. Linearly polarized light, with known s and p components, is directed at the sample surface at specific angles. The reflected light is then collected, and changes in the p and s components are measured. Image used with permission from J.A. Woollam.

This change in polarization is described by the amplitude ratio Ψ, and the phase difference Δ:

$$\rho = \frac{r_p}{r_s} = tan(\Psi)e^{i\Delta} \tag{7}$$

Where ρ is ratio between the complex amplitudes of the s and p components of the reflected light. Amplitude and phase are then derived from the reflection measurements and charted (Figure 4).

Those profiles are strictly dependent on the dispersion profiles of optical parameters such as refractive index and extinction coefficient. Therefore the adjustable optical parameters of a model are adjusted to match the experimental results (Fig-

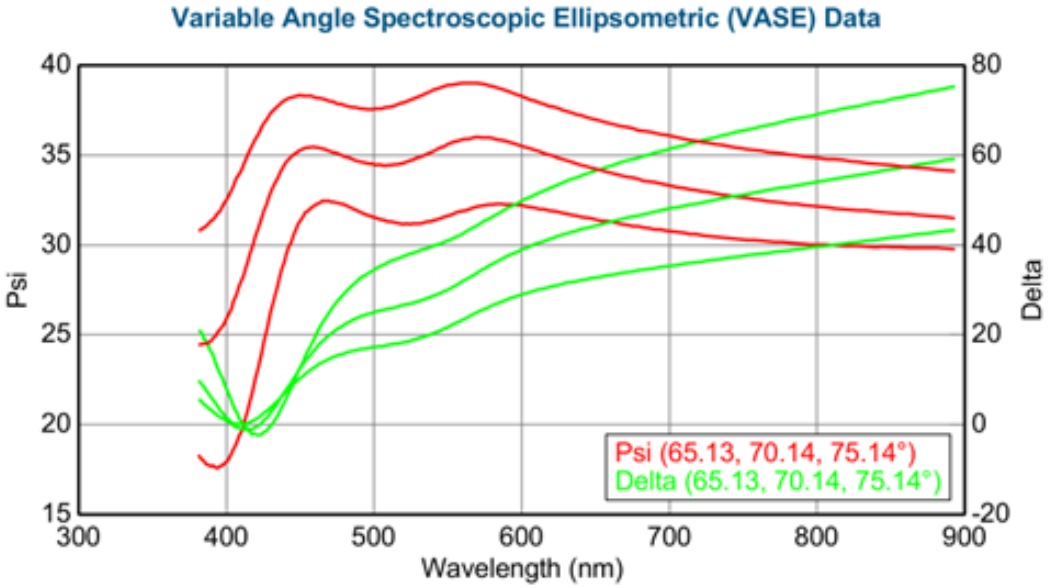

Fig. 4 This is an example of Ψ and Δ measurements taken at three different angles (65°, 70°, and 75°) on a PEDOT sample on a glass substrate. The light source in this specific model of ellipsometer emits in a range between 380 nm and 900 nm.

ure 5). When the mean squared error (MSE) of the fit reach an acceptable value, the model is considered to describe correctly the material investigated, and the optical parameters of the model are considered to effectively describe the optical parameters of the sample.

For a model fit to be acceptable, the model generated data must fit the measured data. MSE should be below 10, but for more complex samples also larger MSE (10-20) are still considered acceptable, provided the fit errors are normally distributed. Additionally, the model should be unique. It is important to test alternative models and varying starting values for the fit parameters to verify model uniqueness; the model should be the simplest possible. Finally, the model and fit parameters must be physically plausible, for instance when a material is transparent (k = 0) the refractive index must increase toward shorter wavelength as shown in Figure 6.

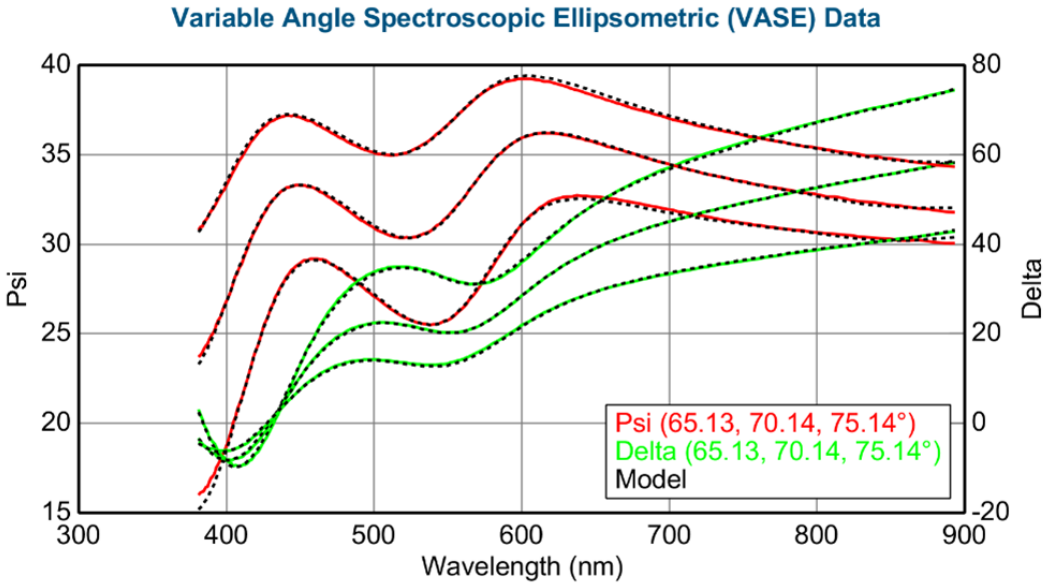

Fig. 5 This shows a comparison of the measured curves with the model of PEDOT described using oscillators. The accuracy of the fit validates the model's effectiveness in describing the material that was measured.

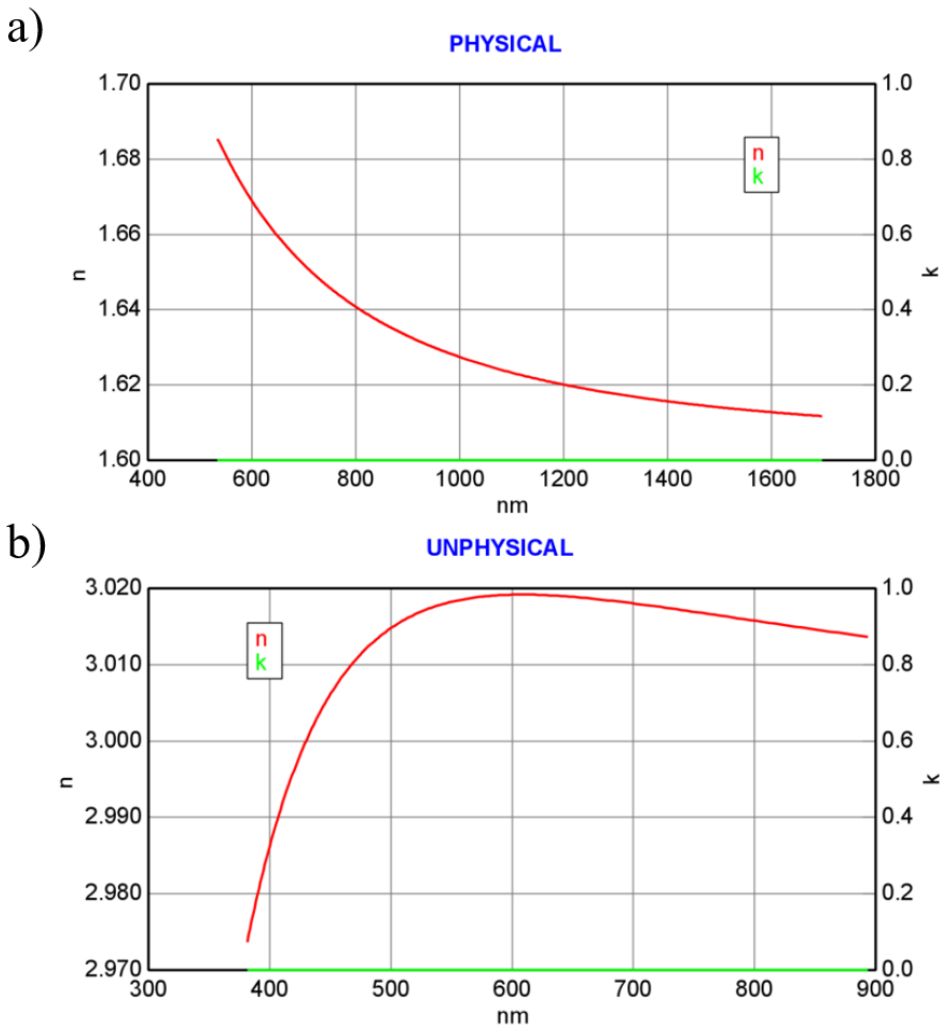

Fig. 6 This image presents an example of a physically plausible model **(a)** and an unphysically plausible model **(b)** used to describe the dispersion function of the refractive index for a material with an extinction coefficient equal to zero. Image used with permission from J.A. Woollam.

0.9.2 Optical Profilometry

Optical profilometry is a technique used for measuring the surface roughness and topography of materials. It operates on the principle of non-contact optical measurement, making it ideal for delicate or soft surfaces. The profilometer projects a light source onto the surface of the material being measured. This light can be in various forms, such as white light, laser, or structured light. The type of light affects the measurement resolution and depth. When the light hits the surface, it interacts with the material's topography. Depending on the surface's features (like bumps, ridges, or indentations), the light will reflect, scatter, or diffract in different ways. The reflected light is captured by a detector, often a camera or a sensor array. This detector records the variations in the light's intensity, angle, or phase, depending on the profilometry technique used. The captured light data is then processed using software to reconstruct a 3D map or profile of the surface. This processing often involves complex algorithms to interpret the light patterns and convert them into accurate topographical data. The resulting 3D map provides detailed information about the surface's characteristics, such as roughness, texture, waviness, and other dimensional features. Two particular techniques have been used in this thesis: confocal and interferometry.

Confocal: in the confocal technique a pinhole, placed in front of the detector, is aligned with the focal point of the lens (confocal). It only allows light from the focal plane of the sample to reach the detector, blocking out-of-focus light from above and below the focal plane. By changing the focus of the objective lens, different planes (slices) of the sample can be imaged. This is termed optical sectioning and allows for the construction of a three-dimensional image of the sample.

Interferometry: In this technique is measured the interference patterns created by the light reflecting from the surface and a reference mirror to the beam splitter, where the two beams recombine. The recombined light creates an interference pattern. When the path lengths of the two beams are closely matched, constructive and destructive interference occurs, resulting in an interferogram. The system captures multiple interferograms at different heights. Software analyzes these interferograms to calculate the height at each point on the sample's surface, constructing a 3D topographical map.

Acronyms

Acronym	Definition
AI	Artificial Intelligence
a-Si:H	Hydrogenated amorphous Silicon
CAD	Computer Aided Design
CCD	Charge Coupled Device
CVD	Chemical Vapor Deposition
EBL	Electron Beam Lithography
ED	Electric Dipole
EQ	Electric Quadrupole
FWHM	Full Width at Half Maximum
ICP	Inductively Coupled Plasma
MD	Magnetic Dipole
MQ	Magnetic Quadrupole
NS	Nanosphere
PDMS	Polydimethylsiloxane
PEDOT	poly(3,4-ethylenedioxythiophene)
Q-factor	Quality factor
RIE	Reactive Ion Etching
RIU	Refractive Index Unit
RMS	Root Mean Square
rpm	rotation per minute
SOI	Silicon Carbide on Insulator

Table 1 Glossary of Acronyms

Chapter 1

Metalenses

In the realm of optics and photonics, the fundamental principle of focusing light has been achieved through the use of conventional lenses for centuries. These optical components, typically composed of materials with distinct refractive indices, manipulate the path of light rays to converge or diverge them, facilitating the formation of real or virtual images. Traditional lenses have undoubtedly revolutionized various fields, from microscopy to astronomy, providing invaluable tools for our understanding of the universe.

However, as science and technology advance, so does the quest for innovation and improved performance. In this quest, we delve into the realm of metalenses, an emerging field at the intersection of physics, nanotechnology, and materials science. Metalenses represent a groundbreaking departure from the traditional paradigm of bulky refractive lenses. They offer unprecedented control over the phase, amplitude, and polarization of light, enabling the creation of ultrathin, planar optical devices with remarkable capabilities.

This chapter explores the concept of metalenses and their role in the manipulation of light. To understand the transition from conventional lenses to metalenses, we will begin by revisiting the fundamentals of traditional lenses, which rely on the principle of phase delay to bend light. As we progress, we will introduce the concept of Pancharatnam-Berry phases, a crucial theoretical framework underpinning the operation of metalenses. The understanding of this phase allows us to unlock the full potential of metalenses in controlling light at the nanoscale.

Furthermore, we will delve into the specifics of metasurface design and fabrication, exploring the intricate physics behind their functioning. With a focus on monochromatic optical beams, we will demonstrate how metalenses can be tailored to efficiently manipulate and focus light, offering advantages over traditional lenses in terms of size, weight, and adaptability.

1.1 How does a lens work?

The fundamental principle behind a lens's operation is the phenomenon of refraction. Refraction occurs when light passes from one medium (e.g., air) into another medium (e.g., glass or another transparent material) with a different refractive index. A lens typically has a curved shape, which can be either convex (thicker in the center) or concave (thinner in the center). Convex lenses are used for converging or focusing light, while concave lenses are used for diverging or spreading light. The curvature of the lens is what causes the bending of light.

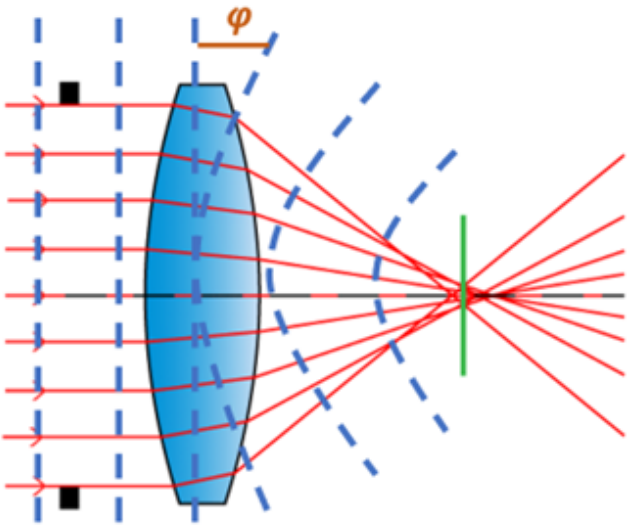

Fig. 1.1 This is a schematic representation of an optical convex lens. The path of light is bent due to the curvature of the wavefront, which is induced by the phase delay of light passing through a medium. The shape of the lens and its thickness determine the focal distance.

The behavior of a lens can be mathematically described using the lens equation:

$$\frac{1}{f} = \frac{1}{v} - \frac{1}{u} \tag{1.1}$$

Where:

f is the focal length of the lens.

v is the distance from the lens to the image formed (positive if the image is on the same side as the outgoing light, negative if on the opposite side).

u is the distance from the lens to the object (positive if the object is on the same side as the incoming light, negative if on the opposite side). The focal length of a lens can be changed by altering its curvature. Thicker lenses have shorter focal lengths, while thinner lenses have longer focal lengths.

1.2 What are the advantages of metalenses?

Lenses suffer from chromatic aberration, which means they bend different colors of light by varying amounts. This results in the splitting of white light into its constituent colors, creating color fringes in images. Chromatic aberration limits the quality of images produced by lenses and requires additional corrective elements, such as multiple lens elements or diffractive optics, to mitigate this effect. Metalenses can be designed to have precise and tailored dispersion properties, which means they can control the way different wavelengths of light are refracted. By engineering the nanostructures on the surface of metalenses, it is possible to create a single, compact, and lightweight element that significantly reduces or eliminates chromatic aberration. Moreover, traditional lenses can be bulky and heavy, especially in optical systems requiring multiple lens elements to achieve various optical functions. This bulkiness limits their applicability in compact devices and lightweight systems. Metalenses are ultra-thin and flat compared to traditional lenses. They achieve the same optical functions as their bulkier counterparts but with significantly reduced size and weight. This makes metalenses ideal for miniaturizing optical systems, such as smartphone cameras, virtual reality headsets, and lightweight imaging devices.

Similar functionalities and benefits have previously been achieved through diffractive or Fresnel lenses, which employ a series of concentric grooves or steps on one surface to create a phase profile capable of focusing or collimating light. However,

the miniaturization of meta-atoms affords greater degrees of freedom, as their nanostructures can assume diverse forms, and allows for the production of thinner devices [22]. This capability enables the engineering of metalenses to achieve enhanced resolution in phase distribution, higher numerical aperture, correction of chromatic aberrations, and an extended depth of focus [23].

1.3 The Pancharatnam-Berry phase

To achieve the realization of a Metalens for focusing a monochromatic laser beam, we've harnessed the principle underlying the Pancharatnam-Berry phase. Unlike conventional lenses that rely on refraction, this particular metalens leverages phase changes. Specifically, the Pancharatnam-Berry phase encompasses the distribution of phase changes necessary to achieve focused beaming at a designated focal distance.

$$\varphi(x,y) = -\frac{2\pi}{\lambda}\left(f - \sqrt{f^2 + x^2 + y^2}\right) \tag{1.2}$$

Where:

λ is the wavelength of the electromagnetic wave passing through the lens.

f is the focal distance of the lens.

x and y are the coordinates inside the lens.

This phase alteration is achieved through nanopillar structures capable of inducing resonances and introducing controlled phase delays. By engineering these nanopillar configurations in a precise manner, we can manipulate the distribution of phase delays, consequently attaining the desired focal distance. Remarkably, shorter or longer focal distances don't require a scaling of the metasurface size, but can be achieved properly engineering the meta-atoms geometry and displacement, as it will be clearer in the following sections.

1.4 Design of a metalens

In the initial stages of metalens development, my primary focus was on the design phase. As previously elucidated, the crux of achieving the focus of an electromag-

netic beam lies in strategically manipulating the distribution of phase delays. This manipulation directly correlates with the geometric attributes of the nanopillars employed in the metalens.

Among these attributes, the height, diameter, and shape of the nanopillars play pivotal roles in dictating the distribution of the confined light field, thereby influencing the magnitude of the phase delay induced. In this specific endeavor, we opted for a cylindrical shape, chosen for its capability to sustain electromagnetic field confinements, which are fundamental in achieving the desired phase modulation.

Regarding the height, it remained a constant parameter due to the uniformity established during the material deposition stage of the fabrication process. Consequently, all fabricated structures maintained identical heights. However, the diameter of the nanopillars emerged as a critical degree of freedom in the design. Utilizing EBL, precise control over the diameter of each individual pillar became feasible, granting the ability to fine-tune the phase delay distribution.

The initial phase of the design process involved rigorous physical simulations using COMSOL software. Through these simulations, we aimed to meticulously assess and characterize the phase delay introduced by varying diameters of the nanopillars (Figure 1.2).

This process enables the correlation of precise phase delays with corresponding diameter values required to achieve those specific delays. Employing the Pancharatnam-Berry phase equation facilitates the assessment of the phase delay distribution necessary to attain a predetermined focal distance for a monochromatic beam with a wavelength of lambda (Figure 1.3).

As an outcome of the preceding simulations, there exists the opportunity to translate the phase distribution into a corresponding distribution of diameter values (Figure 1.4).

Once the diameter distribution has been acquired, the subsequent phase involves the creation of a Computer-Aided Design (CAD). CAD files are digital repositories housing intricate details utilized by computer software to construct two-dimensional (2D) or three-dimensional (3D) models of objects or systems. These files encapsulate geometric specifics such as dimensions, shapes, textures, materials, and other defining characteristics essential to an object's design (Figure 1.5).

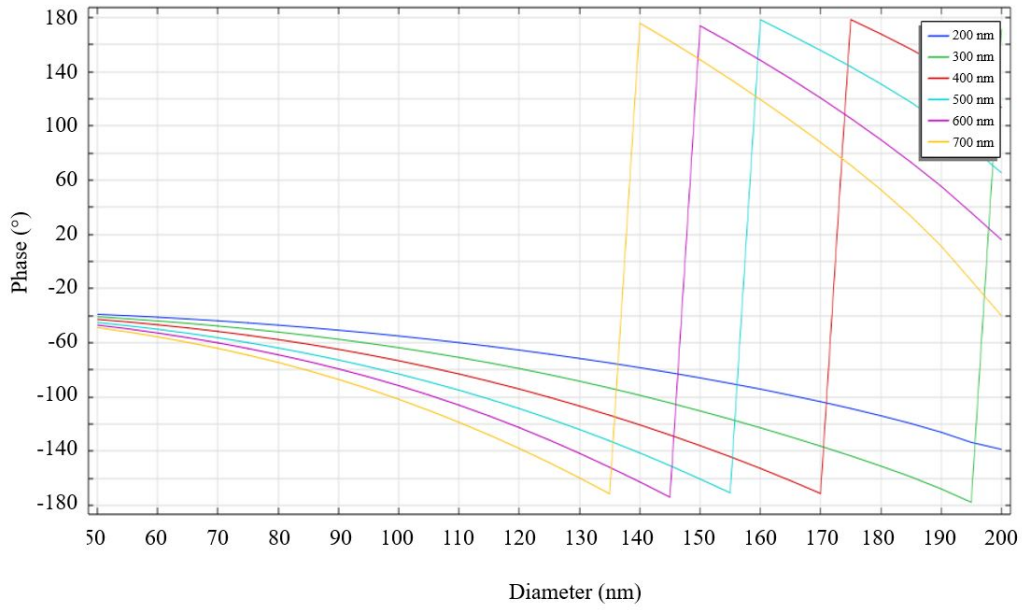

Fig. 1.2 Simulation results of phase delay as a function of diameter introduced by nanopillars with different heights.

In the context of this project, CAD serves as an essential tool in directing Electron Beam Lithography (EBL) during the patterning of the sample. It not only specifies the spatial arrangement for imprinting but also determines the necessary dosage. Given the sheer volume of features—exceeding 10 thousand individual pillars—manual creation of such files becomes impractical. Leveraging Python scripting, it becomes feasible to translate the previously obtained diameter distribution into a CAD file, which subsequently interfaces with EBL for processing. This automated approach streamlines the generation of CAD files, ensuring precision and manageability in dealing with the extensive number of individual nanopillars within the design.

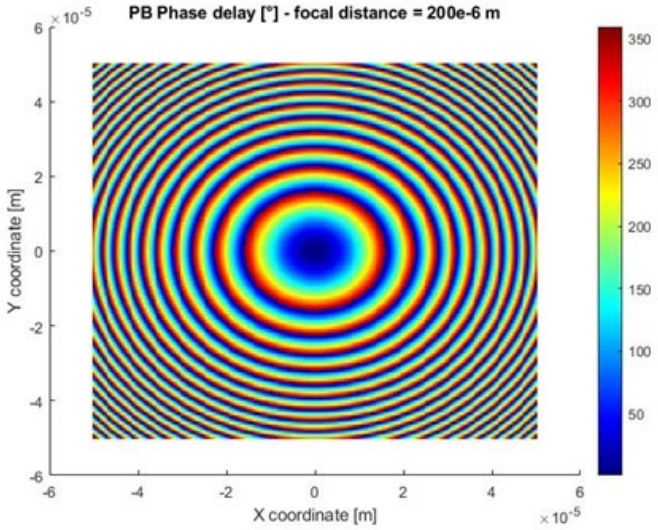

Fig. 1.3 The distribution of phase delay is described by the Pancharatnam-Berry equation, which is used to focus a beam with a wavelength of 663 *nm* to a focal distance of 200 μm.

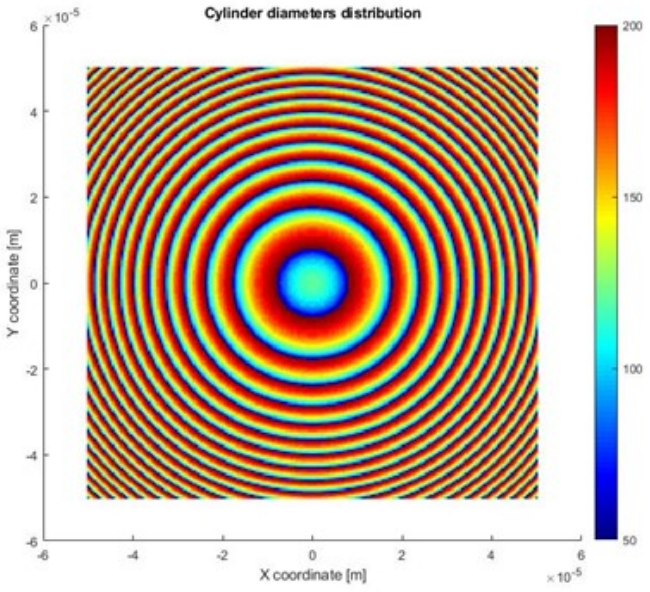

Fig. 1.4 Distribution of nanostructure diameters according to the Pancharatnam-Berry phase equation for focusing a laser beam.

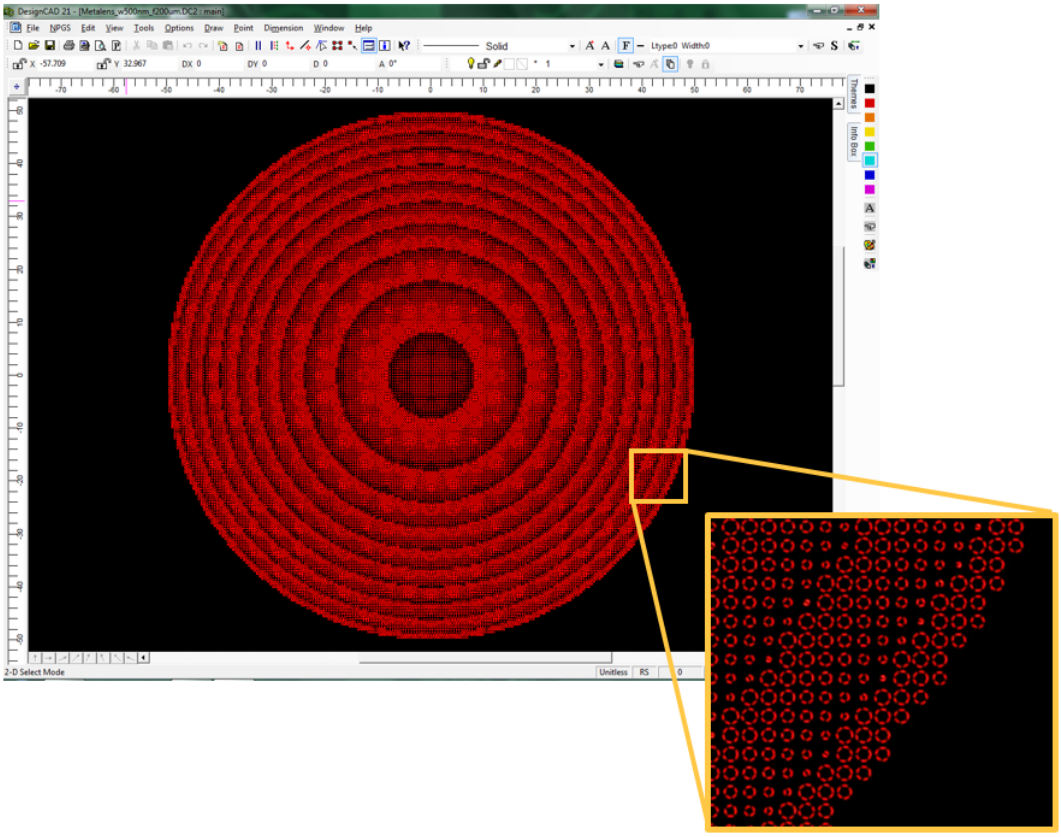

Fig. 1.5 CAD diagram of a metalens used for Electron Beam Lithography (EBL). Each circle represents a solid dot with varying diameters based on its position. The CAD file provides details about the area to be exposed to the electron beam.

1.5 Metalens fabrication

For the fabrication process of metalens, we opted to utilize a glass substrate. This choice provided rigid support without altering the optical properties of the metalens. At the wavelength we worked with, glass proved transparent and minimally absorbent. Before deposition, the samples underwent treatment with oxygen plasma to prepare the surface. This process effectively cleansed the sample of organic residues. The process flow diagram is shown in Figure 1.6.

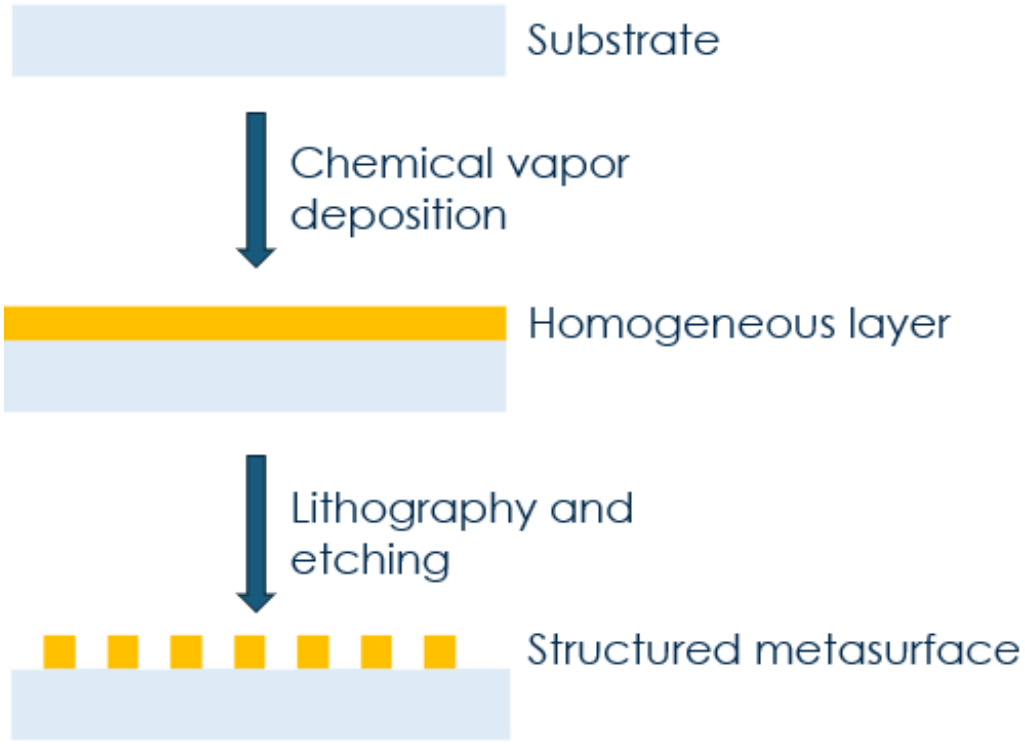

Fig. 1.6 This diagram depicts the process flow for fabricating nanostructures. Initially, the material is deposited using chemical vapor deposition. Then, the resist is exposed through electron beam lithography, and finally, the excess material is removed by dry etching.

On this substrate, I deposited materials characterized by a high refractive index, maximizing the light-material interaction while ensuring low absorption to prevent losses in the metalens. Consequently, we chose amorphous silicon and silicon nitride. In particular, amorphous silicon exhibits a notably high refractive index, typically ranging between 4 and 5 in the visible spectrum. However, this characteristic

is accompanied by increased absorption, rendering amorphous silicon an opaque material. Nevertheless, the planar nature of metasurfaces enables the fabrication of devices with thicknesses on the order of a few hundred nanometers. Consequently, the material thickness falls below the skin depth of the visible spectrum, rendering amorphous silicon suitable for optical applications. Material deposition was executed via ICP-CVD, applying approximately 740 *nm* of material onto the samples.

The subsequent step involved EBL. Prior to exposing the material, an electron resist layer was deposited, a crucial element acting as a mask for the etching phase. Another round of oxygen plasma treatment was essential to enhance surface wettability and optimize resist distribution by reactivating surface free radicals. This step improved the resist's application.

Once the electron resist was applied, the sample was loaded into the vacuum chamber of the EBL system. The vacuum condition was imperative to enhance lithographic resolution, as particles in the chamber could interfere with the electron beam, inducing electron scattering.

Following the exposure of the electron resist, the development process ensued. This process involved immersing the sample in a specific chemical agent that selectively removed either the exposed (in positive resist) or unexposed (in negative resist) resist, thereby revealing the underlying material to be etched.

The etching process employed RIE. This technique involved bombarding the surface with ions generated by an induced plasma and consequently accelerated toward the sample surface. The plasma indiscriminately removed exposed material and resist, albeit at different etching rates. Due to its selective aggressiveness towards the underlying material compared to the resist mask, the resist endured longer, safeguarding the material beneath and preventing its removal.

Upon completion of RIE and removal of residual resist masks, the device was finalized (Figure 1.7). The CAD-provided geometry had been successfully transferred onto the active layer of the sample, which now bore the structured features of the Metalens.

The metalens was characterized using a monochromatic laser beam at the frequency of 633 μm incident perpendicular to the surface of the metalens. Focal planes were captured using a CCD camera to measure the focal distance of 200 μm (Figure 1.8).

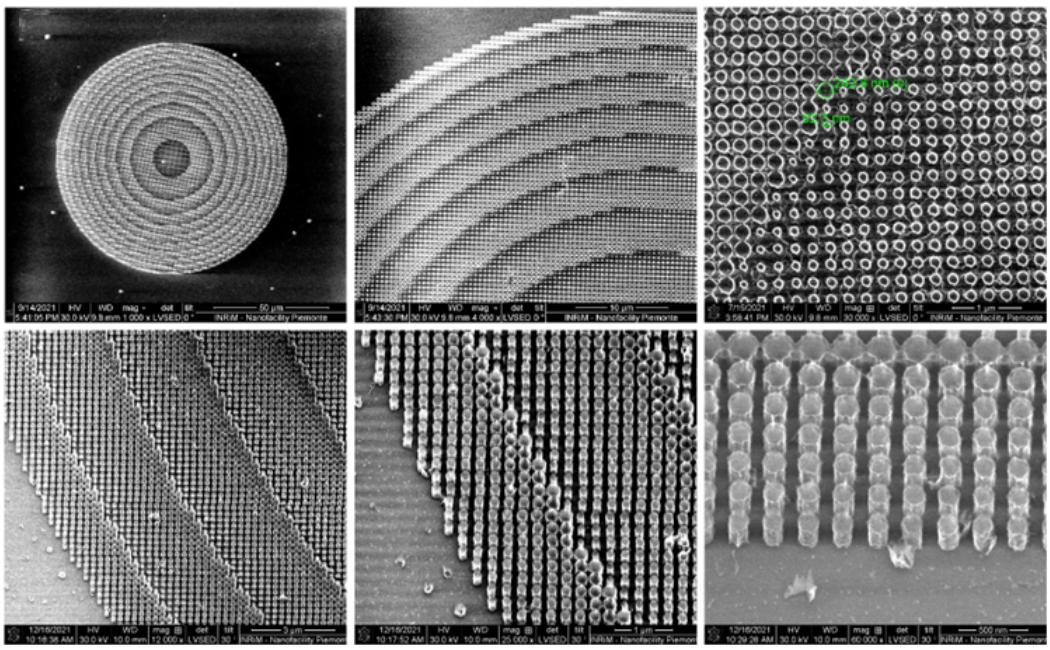

Fig. 1.7 Images captured using scanning electron microscopy at various magnifications of the fabricated metalens. The final nanopillars are composed of hydrogenated amorphous silicon on a glass substrate.

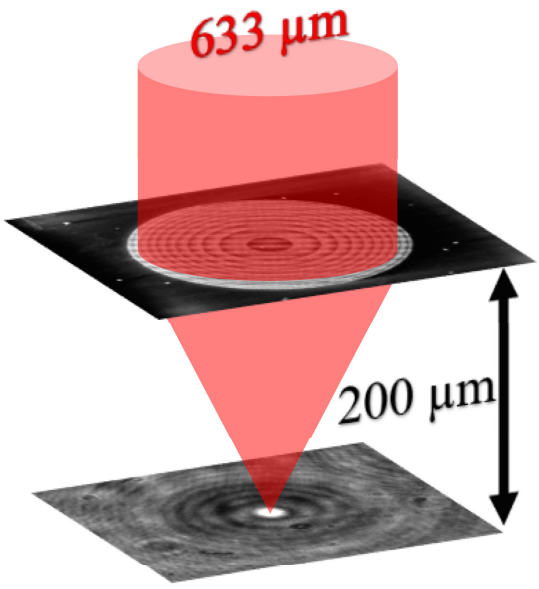

Fig. 1.8 Schematic representation of the metalens functioning. A monochromatic beam at 633 μm is focalized at a focal distance of 200 μm and the focal plane is captured with a CCD camera.

Chapter 2

Large area metasurface

An application of metasurfaces has been shown, where nanopillars can be arranged to create a metalens capable of focusing a laser beam at a specific focal distance. Despite utilizing an extensive array of nanopillars, the resulting metalens is relatively compact, with a diameter of 60 μm. This compact size proves advantageous for certain specialized applications.

However, there is a growing need for larger-scale devices to cater to a wider range of real-world applications. Metasurfaces of smaller dimensions are typically confined to laboratory research or specialized niche uses. In contrast, larger metasurfaces offer potential for integration into mainstream commercial products, including cameras, sensors, and display technologies. The expanded surface area of these metasurfaces enables more extensive manipulation of light, allowing for greater control over key optical properties such as phase, amplitude, and polarization. This capability is particularly advantageous in advanced imaging systems, where large-scale light control can enhance resolution and image quality.

Additionally, larger metasurfaces facilitate easier integration with other optical components, a crucial factor in the development of photonic circuits and systems. In these systems, metasurfaces serve as vital elements, working alongside lenses, mirrors, and other optical components. Economically, the production of larger metasurfaces is more cost-effective, leveraging economies of scale. This aspect is particularly relevant as the demand for photonic devices increases, making the ability to produce larger components in a cost-efficient manner a significant competitive advantage.

Nevertheless, large area metasurfaces encounter a critical challenge: fabrication time. The technique illustrated in the previous chapter, which is based on electron beam lithography, requires that each individual meta-atom be crafted by the electron beam. It becomes evident that this issue escalates with the scaling of metasurface dimensions. Therefore, there is a need to develop a fabrication technique that enables the simultaneous creation of the entire metasurface structure, thereby drastically reducing fabrication time. To this end, nanosphere lithography is proposed.

2.1 Nanosphere lithography

Nanosphere (NS) lithography is a nanofabrication technique with the specific purpose of creating large-area masks used for selective etching of substrates. This method aims to replace EBL, traditionally used for exposing and creating hard masks. It involves spin-coating a monolayer of nanospheres onto the substrate that needs to be etched. This layer acts as a mask, facilitating the formation of cylindrical pillars by projecting the spherical geometry of the nanospheres onto the substrate. Unlike EBL, which is limited in speed due to the need to replicate each pattern element individually, nanosphere lithography allows for the simultaneous creation of the entire mask with a single spin-coating step.

Polystyrene is one of the most commonly used materials for nanospheres. Its uniform size distribution, ease of synthesis, and stability make polystyrene spheres a preferred choice. A popular method for synthesizing polystyrene nanospheres is emulsion polymerization. This technique polymerizes styrene monomers in an aqueous medium, using surfactants to form spherical particles. The size of these nanospheres can be controlled by adjusting various synthesis parameters, such as the concentration of monomers, surfactants, or initiators. Temperature and reaction time are also crucial for determining the size and uniformity of the nanospheres.

2.2 Nanosphere fabrication

The fabrication of a large-area metasurface begins with meticulous surface preparation. It's crucial that the surface is not only cleaned but also has its wettability enhanced. For this process, we subjected the sample – comprising a 154 *nm* layer

of hydrogenated amorphous silicon (a-Si:H) on a glass substrate – to an oxygen plasma treatment. This exposure lasted for 5 minutes, utilizing a power setting of 40 W and an oxygen flow of 50 $sccm$. Although the chamber lacks active temperature regulation, sensors were used to monitor the temperature closely, ensuring it did not substantially surpass room temperature throughout the process.

Nanospheres are typically available in a liquid solution. For our experiment, we applied approximately 80 μL of this solution onto a 2-inch square sample. The even distribution of this solution across the sample is a critical step, as it directly influences the formation of a uniform nanosphere layer. Achieving a single layer of nanospheres is delicate; insufficient rotation and spin-coating time can result in multiple layers, whereas excessively high rotation speeds may prevent the nanospheres from adhering properly to the surface.

To address this, we developed a two-step rotation protocol. The first step involves spinning the sample at 500 rpm for 5 seconds, allowing for an initial spread of the nanosphere solution. The second step ramps up the speed to 3000 rpm for 30 seconds, fostering the formation of a monolayer. This process naturally arranges the nanospheres into a hexagonal cell lattice, creating well-ordered areas known as grains.

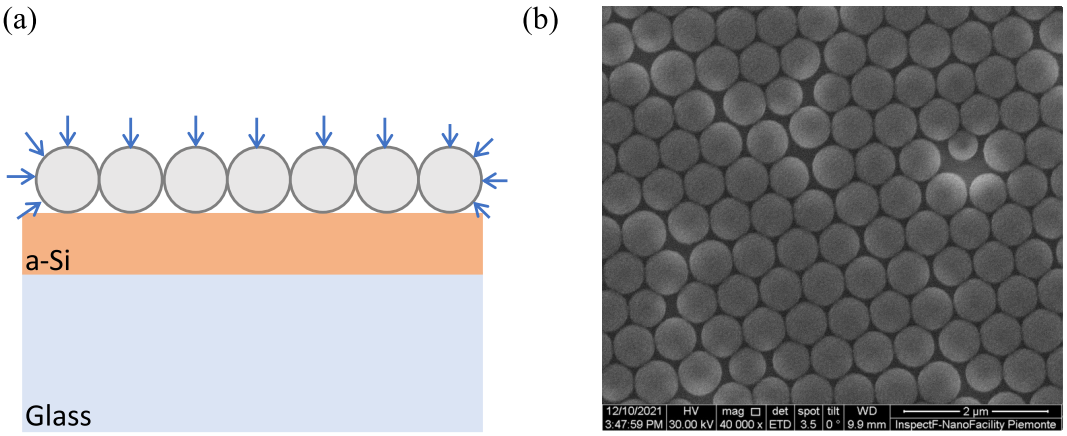

Fig. 2.1 **(a)** Diagram illustrating the process step of nanospheres reduction using Argon plasma. **(b)** Scanning Electron Microscope image of the nanosphere monolayer following spin coating. The pitch is determined by the diameter of the nanospheres.

The initial diameter of the nanospheres, which in this case is 394 nm, is crucial as it determines the pitch of the final structures (Figure 2.1). Before proceeding to the etching stage, it's necessary to fine-tune the diameter of the nanospheres, as this

will determine the size of the eventual cylindrical structures. To achieve this, we exposed the nanospheres to an argon plasma for 6 minutes at a power setting of 75 W. The duration of this exposure is key to accurately reducing the nanosphere diameter, which in this experiment, resulted in a final diameter of 290 nm (Figure 2.2).

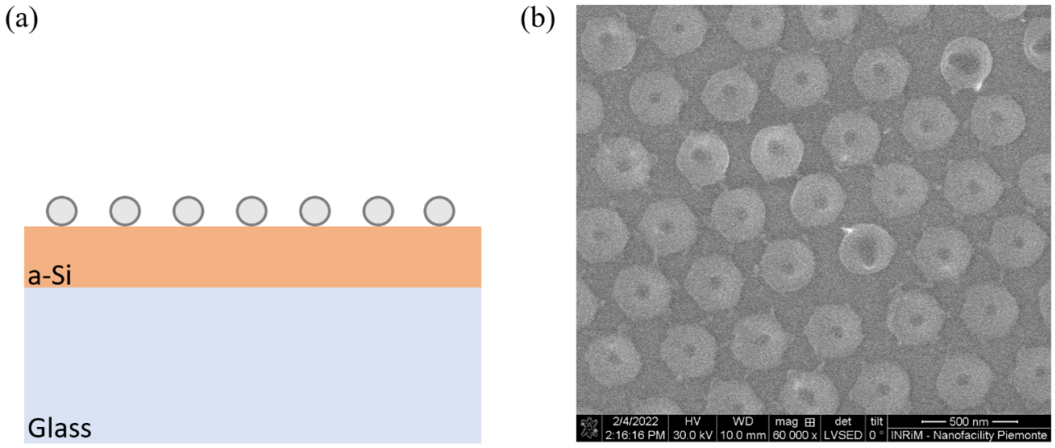

Fig. 2.2 **(a)** Diagram showing the final etching mask created with the reduced nanospheres. **(b)** SEM image of the reduced nanosphere. The reduced diameter of these nanospheres will determine the diameter of the nanopillars.

The subsequent step involves etching the a-Si layer using RIE. My recipe for this process consists in a Pseudo-Bosh etching with a SF_6 and C_4F_8 mixture at the pressure of 10 $mTorr$ and temperature of $10°C$, for 10 minutes of process time. The gas mixture must selectively etch the a-Si while minimally impacting the nanospheres, which serve as a mask. It is crucial to ensure that the etching is vertically oriented, allowing the spheres to be effectively projected onto the layer, thus creating nanopillars. Following the etching process, the NSs can be removed using ethanol (Figure 2.3).

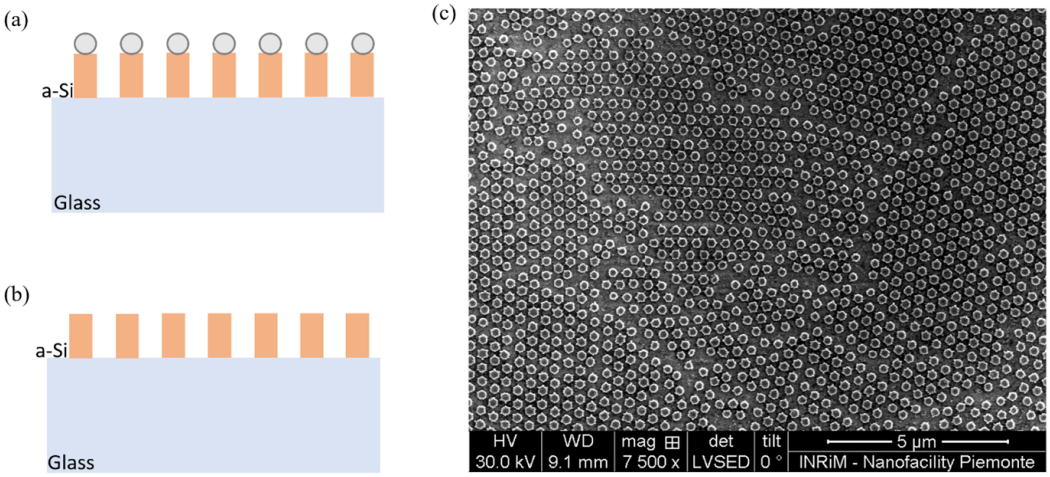

Fig. 2.3 **(a)** Diagram showing the etched material after RIE process. Nanopillars structures developed below nanoshperes. **(b)** Diagram of the final device, cleaned by nanoshperes. **(c)** SEM image of the metasurface, consisting of silicon amorphous nanopillars on a glass substrate.

2.3 Large-area metasurface characterization

The optical properties of the fabricated device have been characterized, specifically measuring its transmission, reflection, and absorption. The measurement setup (Figure 2.4) includes a halogen lamp as a light source, emitting in the visible spectrum, coupled to a fiber optic. The fiber optic's output end is oriented perpendicularly to the device's surface, maintaining a distance of a few centimeters. On the opposite side, another fiber optic, positioned perpendicularly, collects light transmitted through the sample and conveys it to a spectrometer. The input fiber optic features a dual-channel design, enabling it to both emit light and collect reflected light for reflection measurements. Absorption is calculated using the formula:

$$1-(T+R) \tag{2.1}$$

Where T is the transmission and R is the reflection.

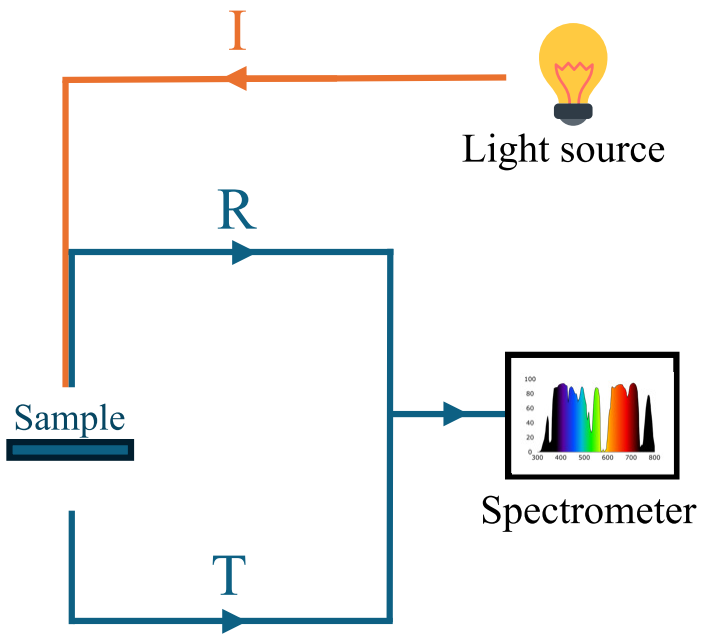

Fig. 2.4 Experimental measurement setup sketch consisting of a fiber optic (I) for the incident light, two fiber optics (R) for the reflected and (T) for the transmitted components, a visible range light source and a spectrometer.

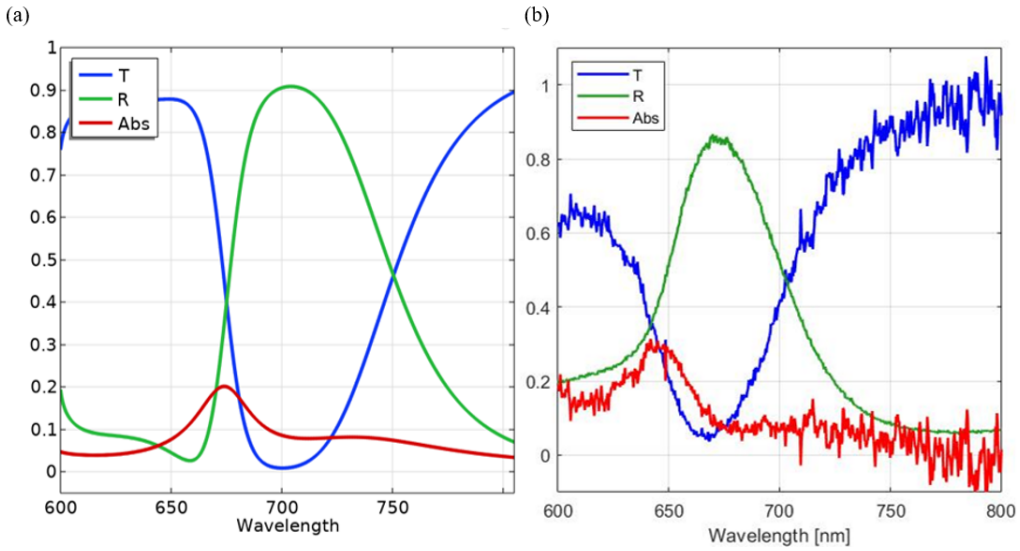

Fig. 2.5 **(a)** Simulation of the transmittance (T), reflectance (R) and absorbance (A) of the metasurface. **(b)** Measurements of the same properties with a spectrometer on the fabricated metasurface.

To provide a benchmark for the experimental measurements, we replicated the metasurfaces using COMSOL Multiphysics and simulated their optical behavior. This simulation included the transmission, reflection, and absorption characteristics, which were then compared with the experimental data. Figure 2.5 presents both the experimental data and the measured results. It is evident that the desired feature has been successfully replicated in the fabricated device. The slight frequency shift can be attributed to minor differences in geometric parameters, due to the challenges in controlling the fabrication process, such as the material deposition thickness and the lateral features during RIE. Additionally, the slight variation in the dimensions of the nanospheres leads to non-uniform pillar sizes. Nevertheless, these parameters can be adjusted to optimize the device's performance for specific applications that require more precise control over the optical behavior in terms of wavelength.

Notably, the experimental results show absorption intensity values below zero in the wavelength range between 750 *nm* and 800 *nm*. This unphysical result is an artifact attributed to the spectral limits of the spectrometer, which exhibits a poor signal-to-noise ratio in this range. Consequently, broad oscillations may yield values below zero when the true signal approaches zero.

Chapter 3

Resonances in nanopillar structures

3.1 Fano resonances in photonic nanostructures

Metasurfaces have reshaped photonics, replacing traditional optics with thin, scalable devices [24]. Comprising dense arrays of nanoresonators, these structures precisely modulate light by varying resonator size, orientation, and material, enabling advanced control over light [25]. This innovation fuels developments in wavefront control [26], structural color enhancement [27], nonlinear optics [28], and quantum optics [29], driven by the need for materials with high refractive indices and nonlinearities [30, 31].

Silicon, silicon nitride, and certain metal oxides dominate these applications due to their optical properties [32–36]. However, diamond's broad band gap and high refractive index make it a prime candidate for hosting color centers and enabling photonics at both classical and quantum levels [37–40]. Despite its potential, diamond metasurfaces are scarce, hindered by challenges in thin-film growth [41–45]. Advances in nucleation methods are overcoming these obstacles, paralleling silicon's integration in photonics through SOI and Silicon Carbide on Insulator technologies [46–48].

This section explores the optical properties of diamond nanopillars on glass, revealing their ability to generate Fano-like resonances with a Q-factor up to $3.5 \cdot 10^5$, a record for dielectric metasurfaces [49–52]. We analyze how pillar height and the surrounding medium's refractive index influence resonance characteristics, demonstrating these metasurfaces' potential as highly sensitive refractive index

sensors, with up to 72.21 nm/RIU sensitivity. This positions diamond metasurfaces as powerful tools for nanoscale light manipulation, enhancing both linear and nonlinear photonic applications.

3.1.1 Method

We utilized COMSOL Multiphysics® 6.0, a finite element method simulation software, to analyze the metasurface's optical behavior in the frequency domain. The study involved simulating an endless array of diamond nanopillars arranged in a square lattice, applying periodic boundary conditions along both x and y axes. Each unit cell, a square-based parallelepiped, included a single pillar on a glass substrate. A schematic representation is shown in Figure 3.1a. The pillars varied in height from 420 *nm* to 660 *nm*, with a fixed diameter $D = 270$ *nm* and pitch $P = 350$ *nm*.

A linearly polarized electromagnetic wave, oriented along the x-axis, was directed perpendicularly from above. By varying the frequency with steps of $\Delta f = 326$ GHz corresponding to a $\Delta\lambda \approx 0.5$ *nm*, we meticulously captured the transmittance profiles. The simulation employed finer step of $\Delta f \approx 10$ GHz corresponding to a $\Delta\lambda \approx 0.002$ *nm* to precisely delineate the narrowest resonances. Transmittance and reflectance were computed using ports at the top and bottom of the setup. Initially, the superstrate's refractive index was set at 1, and later, it was varied up to 1.5. I also incorporated the wavelength-dependent refractive index of diamond from existing literature [53]. Additionally, the study allowed for a detailed examination of the field distribution inside the pillar across various cross sections.

3.1.2 Results and discussion

Figure 3.1b illustrates how varying the height of the nanopillars influences their transmittance. Notably, each transmittance curve features a distinct dip at the resonance wavelength, with the resonance shifting towards longer wavelengths (red-shifting) as the pillar height increases. This height variation significantly alters both the line width and the shape of the resonances. A typical Fano resonance shape [54] is apparent in some profiles (red line), but as the height increases, this asymmetry lessens, and the resonance lines become narrower (orange and yellow lines). Beyond a certain height, the resonance broadens, and the shape becomes a mirror image of

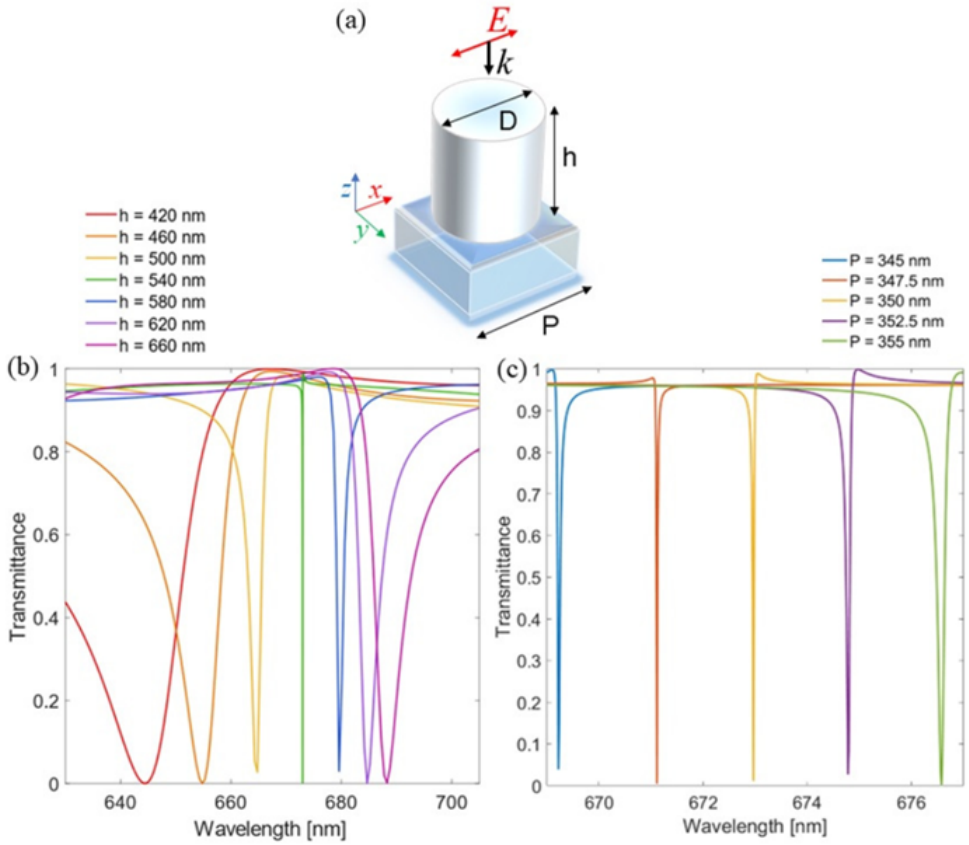

Fig. 3.1 **(a)** Sketch of the unit cell consisting of a diamond nanopillar on a glass substrate ($n = 1.51$). The structure is illuminated by an electromagnetic plane wave with a wave vector travelling perpendicular to the surface and linearly polarized along x. Transmittance profiles as a function of incident wavelength for different values of the pillar's height h **(b)** and pitch P **(c)**.

the earlier profiles (blue, violet, and purple lines). The effect of changing the pillar array period is also examined (as shown in Figure 3.1c), revealing a blue-shift with a shorter period and a red-shift with a longer period, suggesting a near-field interaction between adjacent pillars.

Initially, our examination is centered on the resonance's Q-factor to determine the highest Q-value attainable with the suggested structural design. As depicted in 3.2a, the Q-factor's variation is represented as a function of h. The calculation of the Q-factor is as follows:

$$Q = \frac{\lambda_r}{\Delta\lambda} \tag{3.1}$$

Where λ_r represents the resonant wavelength and $\Delta\lambda$ signifies the Full Width at Half Maximum (FWHM).

At $h = 500\ nm$, the Q-factor stands at $2.9 \cdot 10^2$. However, when h increases to 542 *nm*, the Q-factor escalates dramatically to $3.5 \cdot 10^4$, marking a significant rise of two orders of magnitude. Conversely, for h values exceeding this point, the Q-factor begins to diminish, eventually reverting to $2.9 \cdot 10^2$ as h reaches 600 *nm*.

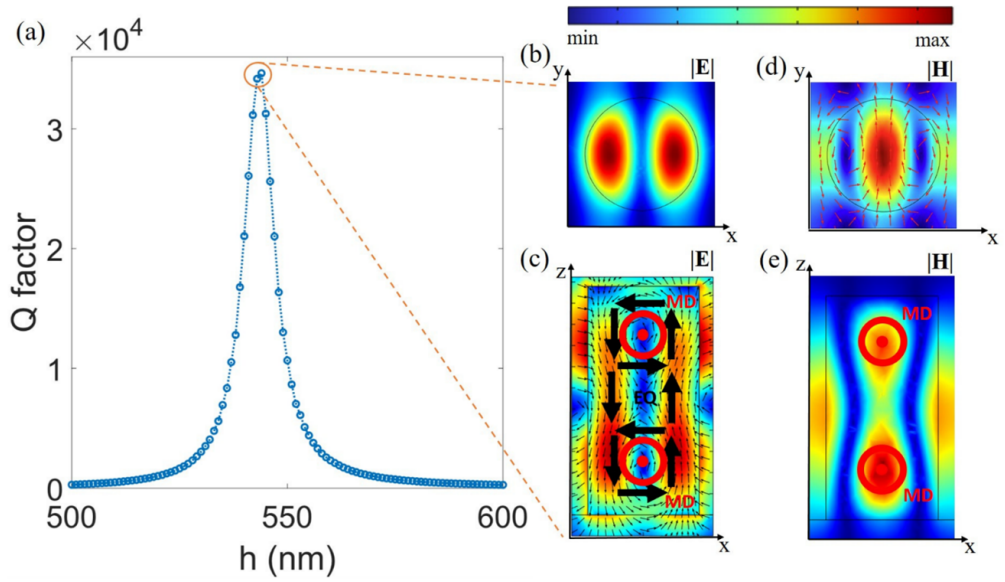

Fig. 3.2 **(a)** Q-factor as function of the height h of the nanopillar, swept from 500 *nm* to 600 *nm*. **(b)**, **(c)** Norm of the electric field distribution in the xy plane at $z = h/2$ **(b)** and in the xz plane at $y = P/2$ **(c)**. **(d)**, **(e)** Norm of the magnetic field distribution in the xy plane at $z = 3h/4$ **(b)** and in the xy plane at $y = P/2$ **(d)**. The arrows represent electric (black) and magnetic (red) field vectors. The fields are extracted for $h = 540\ nm$ and wavelength $\lambda = 672.9\ nm$.

To delve deeper into the resonant characteristics of diamond nanostructures, we analyzed the field distributions at the height (h) that maximizes the Q-factor, as

indicated by the red circle in Figure 3.2a. In this instance, the resonant wavelength is $\lambda = 672.9\ nm$.

The complete elimination of forward scattering seen in transmission spectra, along with the remarkably high Q-factor of the Fano resonances, can be attributed to the interaction between advanced electric and magnetic multipole resonances. This interaction fulfills the generalized Kerker condition, as referenced in sources [55, 56]. A recent study shed light on the significance of multipole resonances in nanopillar arrays by conducting a multipole expansion analysis of the scattered field [57]. Figures 3.2b and 3.2c illustrate the electric field distribution on the xy plane at $z = h/2$ and on the xz plane at $y = P/2$, respectively. The electric field predominantly appears on and around the pillar's side, aligning along the z-axis, which confirms the near-field interaction between the pillars. Examination of the electric field vectors (black arrows in Figure 3.2c) reveals two closed loops, one at the top and one at the bottom of the pillar, both circulating clockwise. These loops create two magnetic dipole (MD) resonances with the MD moment oriented along the y-axis, clearly visible in Figure 3.2d and 3.2e. In Figure 3.2d, the vectors display the MD moment's direction. Between these two MDs, the electric field vectors form an electric quadrupole (EQ) resonance. The intersection of MD (magnetic dipole) and EQ (electric quadrupole) responses fulfills the criteria for the Kerker condition, leading to the complete elimination of forward scattering.

To confirm that the resonance is a Fano resonance, stemming from the overlap of the reflected background field (bright mode) and the MDs and EQs (dark modes) [27], and to understand how the pillar height affects the resonance shape, we applied the Fano formula to the transmittance spectra:

$$T(f) = \frac{(\Omega + q)^2 (1 + q)^2}{(\Omega^2 + 1)} \tag{3.2}$$

Where $\Omega = 2 * \frac{f - f_0}{\gamma}$, including the resonance frequency (f_0) and the resonance width (γ), and q is the Fano parameter [58].

Figure 3.3a illustrates the fitting of three transmittance spectra using this formula. The red ($h = 530\ nm$) and blue ($h = 565\ nm$) lines are slightly off from the peak Q factor condition, while the black line ($h = 542.5\ nm$), achieving the highest Q-factor, is detailed in Figure 3.3b for a closer look at its shape. The black line's FWHM, $\Delta\lambda = 0.02\ nm$, corresponds to a bandwidth of $\Delta f = 14\ GHz$. Figure 3.3c presents

the variation of the two fitting parameters, q (Fano parameter) and γ, with pillar height. This graph distinctly shows a steep change in the Fano parameter from negative to positive values, with the red, blue, and black dashed squares marking the profiles from Figure 3.3a. A Quasi-Lorentzian line shape arises when the resonance width (γ) is at its minimum.

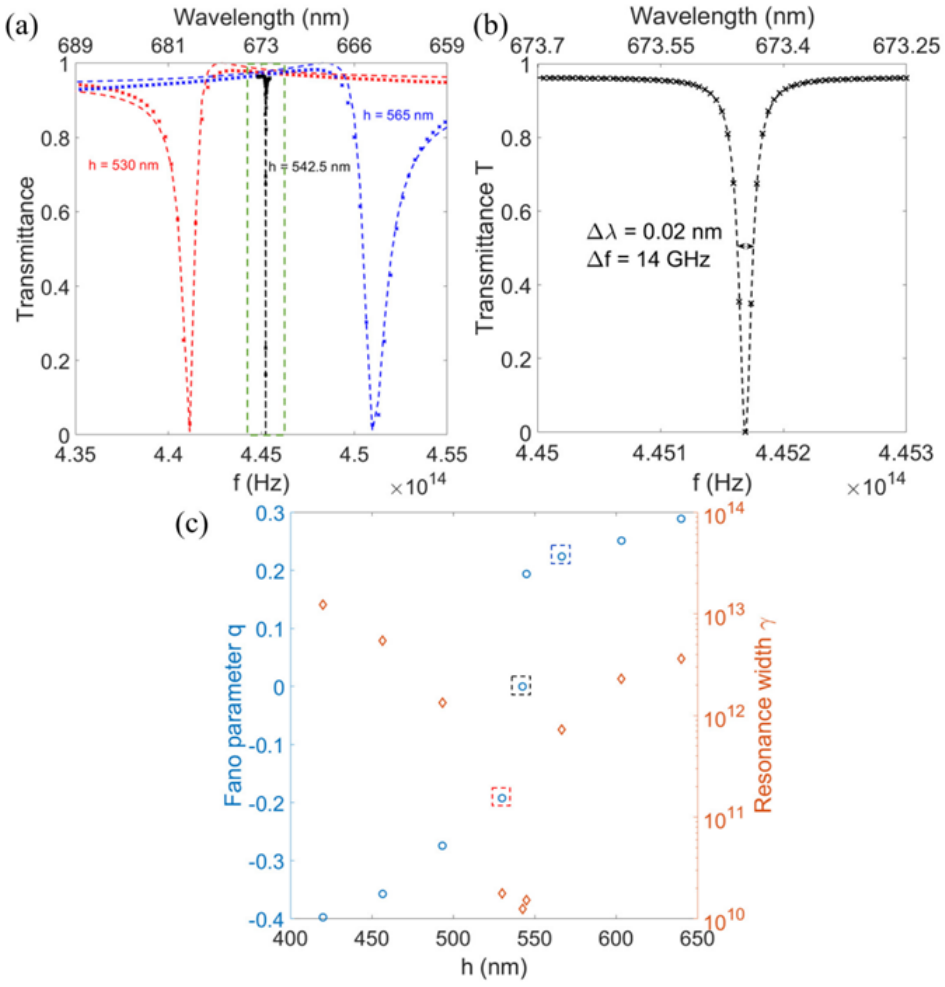

Fig. 3.3 **(a)** Transmittance as a function of the frequency simulated for different heights of the nanopillars: $h = 520$ *nm* (red), $h = 542.5$ *nm* (black) and $h = 565$ *nm* (blue). **(b)** Transmittance as a function of the frequency simulated for nanopillars with height $h = 542.5$ *nm*. Δf is the FWHM of the resonance. **(c)** Fano parameter q and resonance width γ evaluated for different heights of the nanopillars from $h = 400$ *nm* to $h = 650$ *nm*.

For potential sensing applications of the resonant nanopillars [59], we considered a scenario where the diamond-based metasurface is completely submerged in a uniform dielectric material (superstrate domain thickness 1.6 μm). We set the pillar

height at $h = 540\ nm$ and altered the refractive index of the outer layer from 1 to 1.5. The results in Figure 3.4a show a red shift in the resonant wavelength with increasing n. In Figure 3.4b, we plot the resonant wavelength position against the external refractive index and its corresponding Q-factor. The shift in resonance aligns well with a linear function (RMS error = 0.047) with a slope $S = 72.21\ nm/RIU$. The Q-factor peaks at $3.5 \cdot 10^5$ when $n_{sup} = 1.25$, equivalent to a FWHM $\Delta\lambda = 0.002$ nm. Considering the FWHM as the system's resolution limit, we deduce that the metasurface can distinguish refractive index changes as small as $4.2 \cdot 10^{-4}\ RIU$ near an external refractive index of 1, and up to $2.73 \cdot 10^{-5}\ RIU$ when n_{sup} is around 1.25, as calculated from $\Delta n = \frac{\Delta\lambda}{S}$.

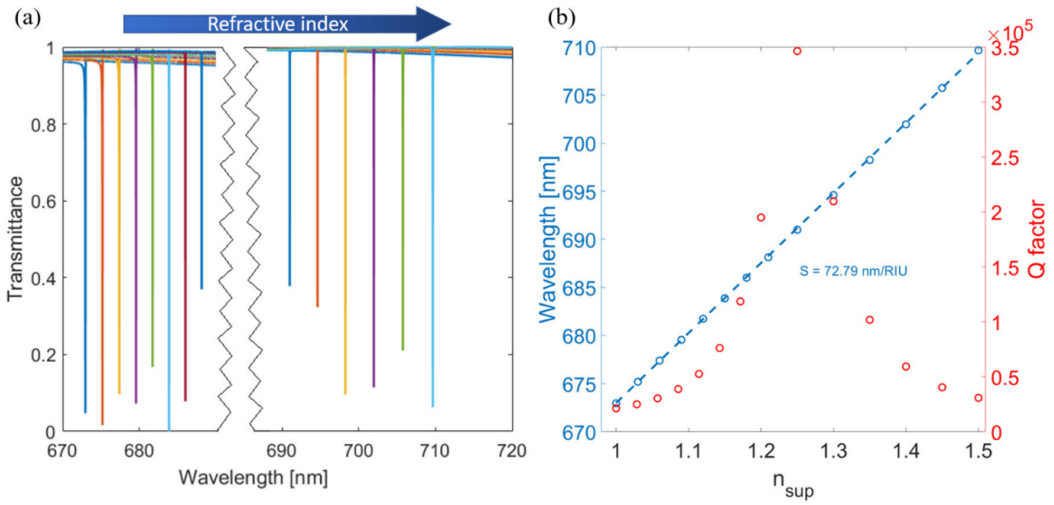

Fig. 3.4 **(a)** Transmittance spectrum calculated for different refractive index values of the surrounding medium, varying from 1 to 1.5. **(b)** Resonant wavelength as a function of the refractive index of the external medium (blue data, left axis) and Q-factor of the resonance (red data, right axis). The blue data are well fitted by a linear function (blue dashed line) whose slope is $S = 72.21\ nm/RIU$.

3.2 Multipolar analysis

Engineering dielectric thin films for light scattering has enabled advancements across various optical technologies, from replacing traditional optics with flat elements to applications in wavefront shaping, lasing, color production, sensing, modulation, and quantum optics [60–71]. The interest in dielectric metasurfaces [24, 72, 73]

from both academia and industry [74] has spurred efforts to design subwavelength elements for customized light interaction [75, 76], including the use of AI for optimizing designs [77–79]. Challenges in fabrication, especially for visible light applications, have prompted a shift towards cost-effective, large-scale production methods [80–82].

This section focuses on dielectric metasurfaces operating on Mie resonances in the visible spectrum, aiming to utilize and combine these resonances for directional scattering control and high-Q Fano resonances [83–86]. We explore the resonant behavior of a dielectric resonator lattice, particularly the non-local effects of multipolar resonances and their lattice constant dependency. We also demonstrate a design capable of high-Q Fano resonances, promising for light modulation and tunable filters. The advantage of this approach lies in the potential for scalable, cost-effective fabrication using self-assembling techniques, offering significant benefits for industrial application of metasurface-based optics [87–92].

3.2.1 Materials and methods

The optical characteristics of the metasurface were examined using the RF module in the Frequency domain of COMSOL Multiphysics® 6.0. The structure modeled for simulation is depicted in Figure 3.5a: it consists of a square array of cylindrical nanopillars, each with a diameter of 270 *nm* and a height of 540 *nm*. These nanopillars have a complex refractive index ($n = 2.4$, $k = 1 \cdot 10^{-3}$), are positioned on a non-absorptive glass substrate ($n = 1.51$ [93]), and are encased in air ($n = 1$). The setup is exposed to a plane wave striking perpendicularly on the surface, with polarization along the x-axis. We varied the free-space wavelength from 640 to 700 *nm*, and for each wavelength, we calculated the reflectance, transmittance, absorbance, the electric field distribution, and the contributions of various multipoles to the scattering cross-section. To replicate the lattice structure, periodic boundary conditions (Floquet periodicity) were applied along the x and y axes. The lattice constant was altered to explore its impact on the metasurface's optical response, while other geometric parameters remained constant.

3.2.2 Fano resonances

Initially, we evaluated the transmittance, reflectance, and absorption spectra around the resonant frequency for various lattice constant values (P) as shown in Figure 3.5b-g. These graphs reveal the presence of Fano resonances in the cylindrical structures, leading to reduced transmittance at the resonant wavelength. These resonances are similar to those identified in recent research focusing on ideal, non-lossy nanopillars [94]. By incorporating a complex refractive index in our model, we observed enhanced absorption within the nanopillars, indicating intensified light-matter interactions. Specifically, as P nears 350 nm, there's a red-shift in resonance and a spike in absorption to nearly 40%, with a corresponding decrease in transmittance. At $P = 350$ nm, the resonance weakens significantly, and absorption drops below 10%. Increasing P further elevates both absorption and the dip in transmittance, reaching nearly zero transmittance at $P = 380$ nm. The typical asymmetry of Fano resonances, characterized by the Fano parameter [95], shifts directionally when P surpasses 350 nm.

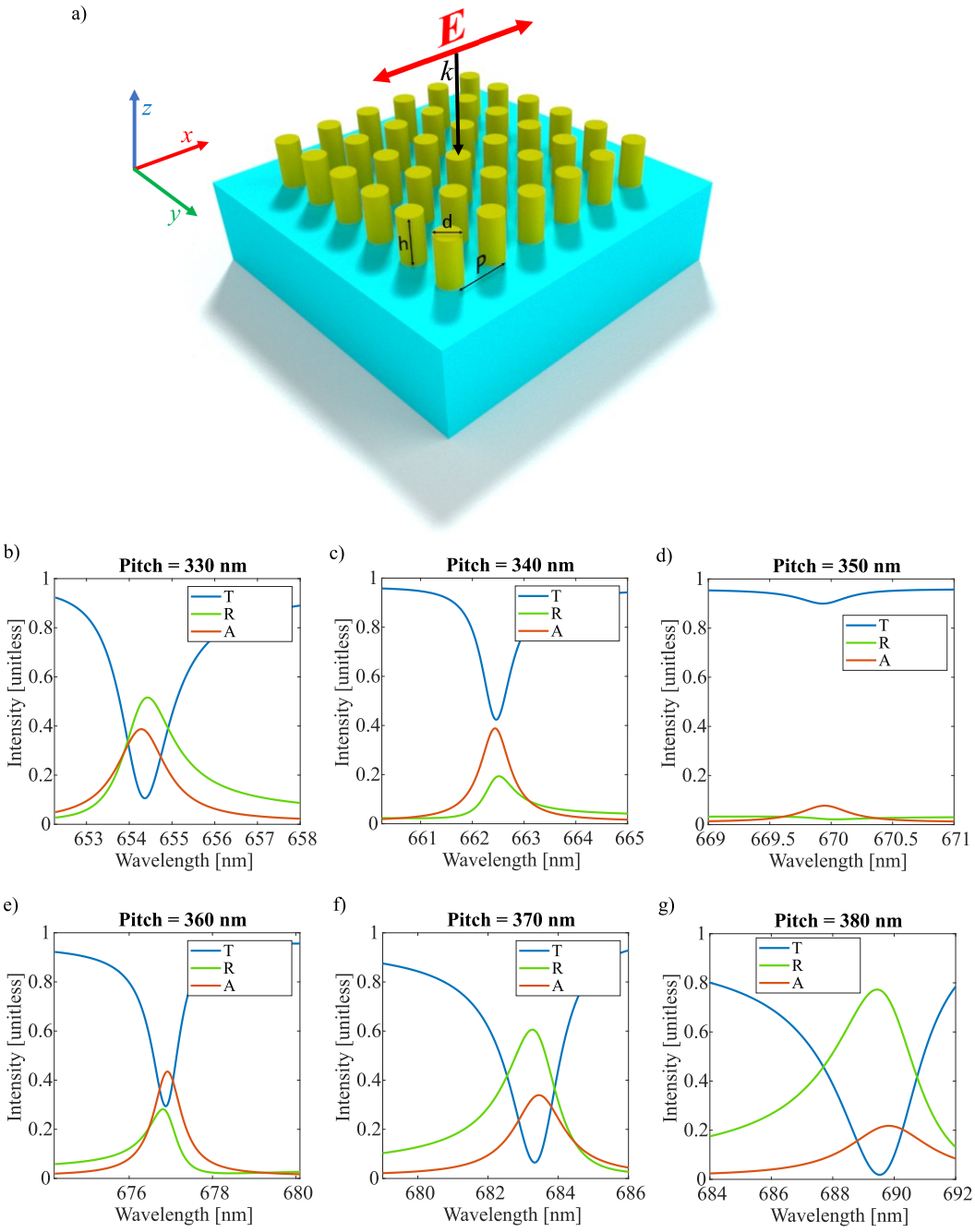

Fig. 3.5 **(a)** 3D schematic of the simulated metasurface. **(b-g)** Graphs showing transmission (blue line), reflection (green line), and absorption (red line) as functions of wavelength for the metasurface, with pitches ranging from 330 *nm* to 380 *nm*.

3.2.3 Multi polar expansion

To delve deeper into the metasurface's resonant behavior, we represented the scattered field as a composition of fields generated by multipolar sources, in line with Mie theory [96]:

$$\mathscr{C}_{sca}^{total} = \mathscr{C}_{sca}^{ED} + \mathscr{C}_{sca}^{MD} + \mathscr{C}_{sca}^{EQ} + \mathscr{C}_{sca}^{ME} + ... \tag{3.3}$$

Here, the total scattering cross section is expressed as a sum of contributions from electric and magnetic dipoles (ED, MD), quadrupoles (EQ, MQ), and higher-order multipoles. Each multipole's individual contribution was calculated as per recent research [97, 98]. This analysis shows MD and EQ resonances contribute most to the scattering cross section, with their spectral position and intensity varying with lattice constant changes (Figure 3.6). For instance, Figure 3.6a shows at $P = 330$ *nm*, the dip in transmittance correlates with a boost in total scattering cross-section, predominantly due to EQ resonance (about 50% of the total) and a substantial MD contribution (around 25%). ED and MQ resonances also strengthen, but their impact on the scattering cross-section remains below 15%. Increasing the lattice constant to $P = 340$ *nm* (Figure 3.6b) results in a red-shift of resonant modes and a narrowing of lineshapes, with changes in EQ and MD intensities.

This trend persists with a further increase in lattice constant to $P = 350$ *nm* (Figure 3.6c), where EQ contribution decreases to 40% and MD rises to 30%. Increasing P by an additional 10 *nm* (Figure 3.6d) leads to almost equal contributions from EQ and MD to the total scattering cross section, and with further increase in P (Figure 3.6e-f), MD becomes dominant.

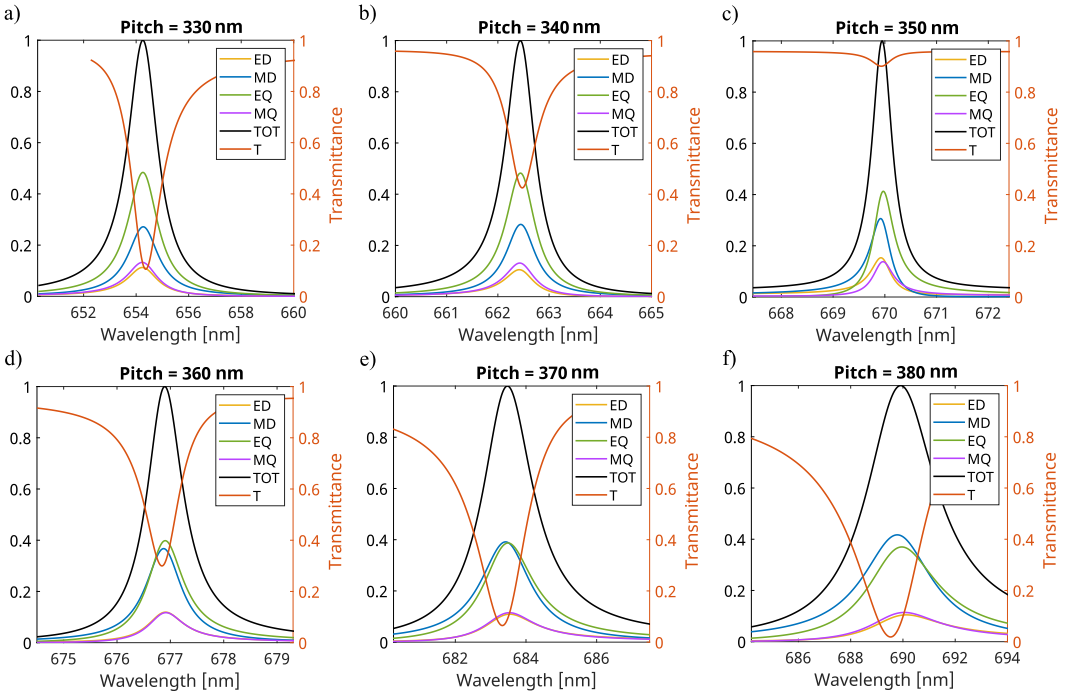

Fig. 3.6 **a-f** Relative intensity of contributions from different multipolar resonances, including the electric dipole (ED), magnetic dipole (MD), electric quadrupole (EQ), and magnetic quadrupole (MQ), as well as the total sum of all contributions (TOT), assessed over a range of pitch values from 330 *nm* to 380 *nm*. On the left axis the transmittance profile (T) is reported in red for reader's convenience.

3.2.4 Field patterns and Q-factor

Examining field patterns within the nanopillars helps understand these multipolar resonances. The false color maps at the top of Figure 3.7 display the electric field distribution's absolute value, normalized with respect to the incident field, for three representative P values (330, 350, and 380 *nm*). The normalized black arrows indicate the electric field orientation. The bottom row sketches the virtual multipoles excited within the pillar, with transparency adjusted to emphasize individual multipolar resonance contributions. At $P = 330$ *nm*, the field distribution features two main lobes along the pillar, representing the EQ, and two weaker loops at the pillar's top and bottom, observed through black arrows. At $P = 350$ *nm*, although the EQ is visible, field enhancement is much reduced. At $P = 380$ *nm*, the two loops generating the MD resonance become more evident, while the EQ field diminishes.

The short distance between the pillars creates an additional cavity between them. This cavity sustains field confinement, generating high intensity near-field interactions among the pillars. As the width of this cavity depends on the distance between pillars, variations in pitch strongly influence the near-field distribution. We believe this contributes to the resonant frequency's dependency on the pitch value of the metasurface.

The lattice constant's influence on resonances is further evident in the Q-factor variation (Figure 3.8a), with a peak value of about 1400 for $P = 350$ *nm*. This peak occurs even as the effects on transmittance (Figure 3.6) and field enhancement (Figure 3.7) are relatively weak.

The shift in spectral position of multipolar resonances with varying lattice constant is further illustrated in Figure 3.6. Figure 3.8b presents the difference in scattering cross section between EQ and MD resonances near the resonance wavelength. At $P = 330$ *nm*, the lineshape is positive and symmetrical, indicating spectral dominance of EQ resonance. Increasing P to 340 *nm* narrows and asymmetrizes the lineshape, which becomes more evident at $P = 350$ *nm*, showing a negative peak at shorter wavelengths and a positive one at longer wavelengths, indicating a smaller redshift for MD compared to EQ. Further increasing P enhances this spectral separation, while broadening the lineshape.

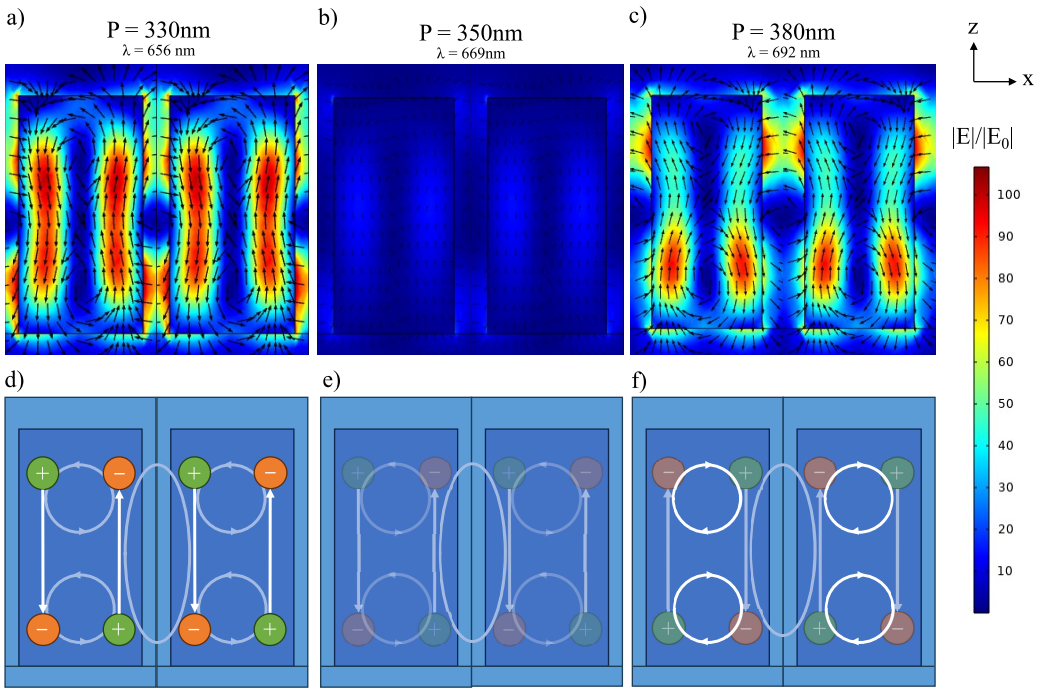

Fig. 3.7 (**a-c**) Norm of the electric field intensity on the XZ plane, passing through the center of a pillar and one of its near-neighbors. The black arrows indicate the orientation of the electric field component on the XZ plane. The electric field has been evaluated for pillars with three different pitches P(**a**)330 *nm*, (**b**) 350 *nm*, and (**c**) 380 *nm* and at their corresponding resonant wavelengths λ (**a**) 656 *nm*, (**b**) 669 *nm*, and (**c**) 692 *nm*. (**d-f**) Schematic representation of the multipole displacement within the pillars. Dipoles with more intense coloring indicate a higher contribution for that specific combination of pitch and wavelength (λ).

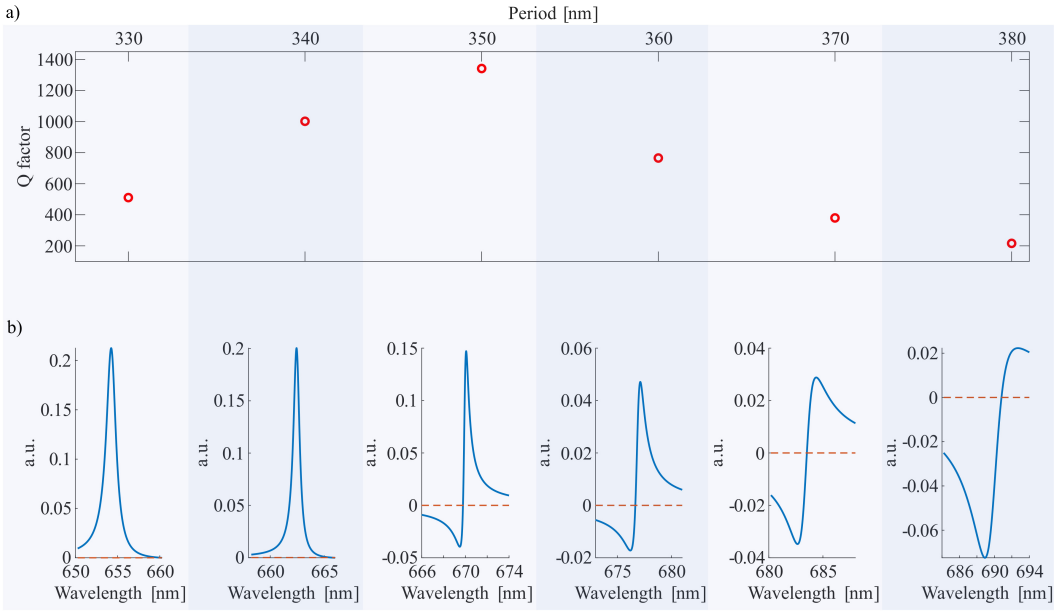

Fig. 3.8 (**a**) Quality factors of the resonances for pillars with pitches ranging from 300 *nm* to 380 *nm*.(**b**) Difference in the scattering cross-sections of the Electric Quadrupole (EQ) and Magnetic Dipole (MD) for the corresponding pitches (blue line). The red dashed line highlights the zero value.

3.3 Metasurface fabrication

We commenced the manufacturing of the device that was previously simulated. Our initial strategy involved replicating the structures using silicon-enriched Si_2N, which not only offers a favorable refractive index but also allows for a more straightforward processing method compared to diamond. To deposit 540nm of Si_2N on a glass substrate measuring 1"x1", we utilized ICP-CVD. Following this, EBL was employed to expose the resist, facilitating the creation of nanopillars with a diameter of 225 *nm* and a pitch of 326 *nm*. Subsequently, we patterned the Si_2N using RIE with a mixture of SF_6 and C_4F_8, setting the ICP power at 1200 W, RF power at 30 W, and chamber pressure at 10 *mTorr*. The plate temperature was maintained at 10°C to enhance the etching efficiency.

The completed device is depicted in Figure 3.10a. It comprises an array of nine pixels, each with a patterned area of 100 $\mu m \times 100\ \mu m$. The pixel dimensions and their placement were meticulously designed to align with the beam spot used for characterization. These can be visually identified due to diffractive effects. Each pixel is designed to be nominally identical, with repetition serving to increase the likelihood of producing a device free from defects or impurities, which are commonly found on the surface. Despite the challenges in fabrication, Figure 3.9 presents our initial test of silicon nitride nanopillars. We succeeded in fabricating separated nanopillars in Si_2N, achieving precise control over their cylindrical shape. The height, diameter, and spacing (pitch) were accurately obtained.

The transmittance of the fabricated device was assessed using the measurement setup previously shown in Figure 2.4. Figure 3.10 illustrates the initial stages of characterizing the metasurface's transmittance. The resonances induced by the nanopillars are distinctly observed, with transmittance significantly reduced at frequencies of 520 nm, 575 nm, 640 nm, and 750 nm. Beyond these resonance frequencies, the transmittance remains exceptionally high, especially in the range between 625 nm and 800 nm, where it approaches 90%. Future work will concentrate on creating a fully operational device.

This initial endeavor to fabricate a metasurface capable of sensing the refractive index of its surroundings has shown promising results. Nonetheless, substantial efforts are necessary to refine the manufacturing process and enhance the precision of the nanostructures' dimensions.

a) b)

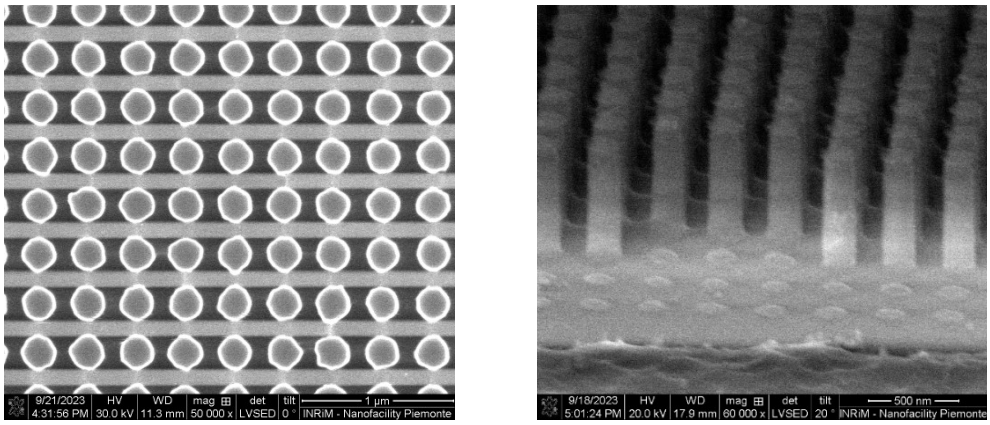

Fig. 3.9 (**a**) SEM image of the fabricated Si_2N metasurface, featuring nanopillars with a height of 540 *nm*, diameter of 225 *nm*, and pitch of 326 *nm*. (**b**) SEM image of the same structures with a tilt angle of 20°.

a) b)

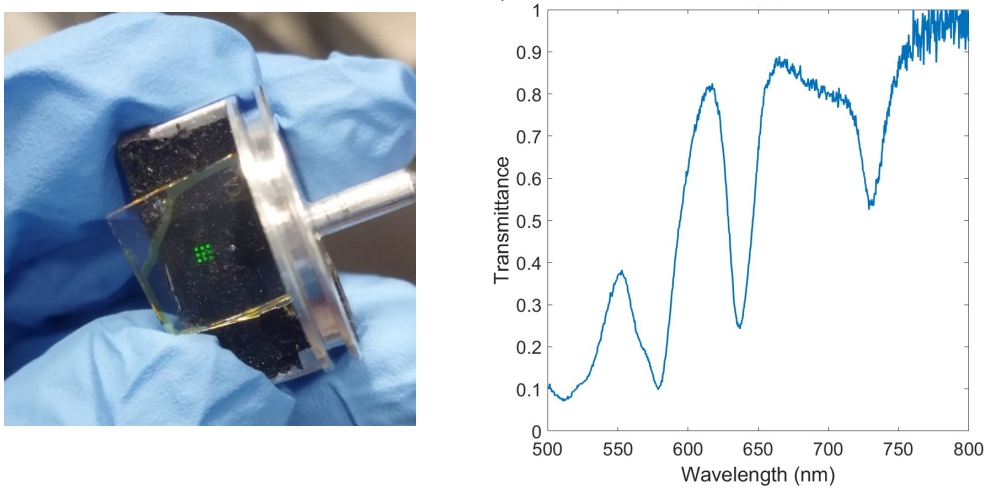

Fig. 3.10 (**a**) Sample analyzed. Each pixel represents a metasurface with a patterned area of 100 μm $\times$100 μm. (**b**) Transmittance measurement obtained using a spectrometer, with the metasurface illuminated perpendicularly using a mercury (Hg) lamp.

Chapter 4

Organic metasurfaces

In the preceding chapters, we explored devices characterized by their use of dielectric materials. This choice was driven by dielectrics' high refractive index, generally low losses, and the reliability and reproducibility of their fabrication processes, making them excellent candidates for such applications. However, dielectrics are insulators by nature, rendering them unsuitable for applications requiring electrical connections. In such cases, metallic materials become the preferred choice due to their excellent electrical conductivity. However, this comes with a downside: metals exhibit high losses, particularly in the visible range, which significantly diminishes the performance of devices like optical metasurfaces when they are used.

Organic materials, however, show promise in addressing these issues. Despite not having an exceptionally high refractive index, organic materials can maintain low losses even in the visible spectrum, where they can sometimes be transparent. Their real benefit lies in their ability to retain optical properties while offering moderate electrical conductivity. This dual capability allows for the simultaneous manipulation of light using nanostructures and the establishment of electrical connections.

In this chapter, I will discuss the application of a specific organic material, poly(3,4-ethylenedioxythiophene), or PEDOT, in designing and fabricating an optical modulator. This approach offers the advantage of lower optical losses compared to traditional modulators that use metallic structures.

4.1 Material synthesis

PEDOT is a conducting polymer widely used due to its excellent electrical conductivity, stability, and transparency in its doped state. The synthesis of PEDOT often involves oxidative polymerization of 3,4-ethylenedioxythiophene (EDOT) monomer.

There are several methods for synthesizing PEDOT, including chemical polymerization in solution and vapor phase polymerization. The synthesis process can be modified by incorporating different dopants to enhance the polymer's properties for specific applications. Here, we'll outline the synthesis processes involving vapor phase polymerization with iron tosylate and liquid phase polymerization with vanadium oxide as dopants. The synthesis process is illstrutated in Figure 4.1.

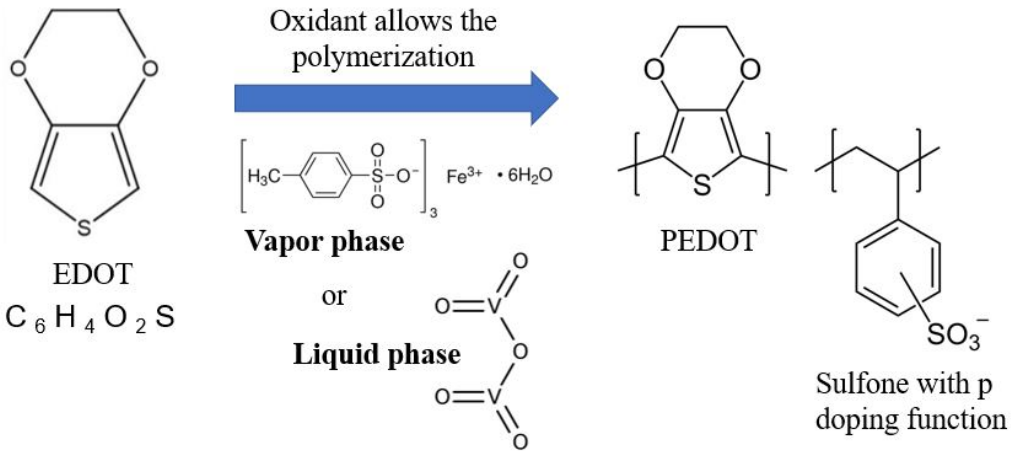

Fig. 4.1 Scheme of the synthesis process for PEDOT with liquid phase and vapor phase methods.

4.1.1 Vapor Phase Polymerization with Iron Tosylate

The process begins with the vaporization of the EDOT monomer. This can be achieved by heating the monomer in a chamber until it vaporizes. The vaporized EDOT is then introduced into a reaction chamber containing a substrate coated with an oxidizing agent, in this case, iron(III) p-toluenesulfonate (iron tosylate). The chamber is maintained at a controlled temperature to facilitate the polymerization process. As the polymerization occurs, the iron tosylate acts as both the oxidant

and dopant, incorporating into the growing PEDOT chains. This doping process enhances the electrical conductivity of the PEDOT. The result is a thin, conductive film of PEDOT doped with iron tosylate on the substrate. The film can be further processed or transferred to another surface if needed.

4.1.2 Liquid Phase Polymerization with Vanadium Oxide

A solution of EDOT monomer is prepared in a suitable solvent. Vanadium oxide, serving as the oxidant and dopant, is also dissolved in the solution to create a mixture. The solution is then subjected to oxidative polymerization conditions. This can be done by heating the solution or using a catalyst to initiate the polymerization of EDOT, with vanadium oxide facilitating the oxidation of the monomer to form PEDOT chains. During polymerization, vanadium oxide incorporates into the PEDOT chains as a dopant, enhancing the material's conductivity. The polymerization is instantaneous and the liquid oxidant solution is homogeneously spread on the surface by spinning.

Both these processes can be optimized to produce PEDOT with desired properties for various electronic and optoelectronic applications.

4.2 Study of the material

The initial step in creating optical devices involves conducting a physics simulation to establish the necessary fabrication parameters. These parameters are critical for achieving desired behaviors and light modulation. The simulation requires knowledge of the electrical and optical properties of the materials used. This information is essential for accurately computing the physical equations that depict the phenomena within the system under study. Precisely understanding these physical properties can be challenging, particularly when dealing with exotic and uncommon materials. While it's relatively easy to find extensive information on common materials like amorphous silicon, comprehensive studies on all organic materials are scarce, especially when their properties are highly dependent on the synthesis processes.

For this reason, it has been necessary to conduct thorough characterizations of PEDOT before utilizing it in fabrication. This includes measuring its electri-

cal properties and optical parameters, such as the refractive index and extinction coefficient.

4.2.1 Electric properties

The electrical properties, particularly conductivity, were measured using sheet resistance measurements. Sheet resistance helps determine the resistance of thin films and can be measured using a four-probe technique (Figure 4.2). This technique involves contacting the film's surface with two pairs of electrodes. A current of varying values is applied between the first external pair of electrodes, while the voltage is measured using the internal pair of electrodes.

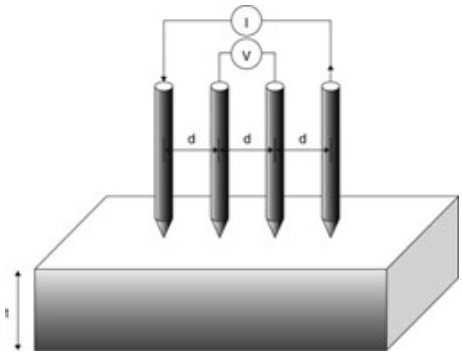

Fig. 4.2 Schematic representation of the four probes station for the measurement of the sheet resistance of thin films.

The sheet resistance can be calculated using the following equation:

$$R_s = \frac{\pi}{\ln(2)} \frac{\Delta V}{I} = 4.53236 \frac{\Delta V}{I} \tag{4.1}$$

Using this technique, we were able to measure the sheet resistance of different PEDOT compositions to identify the one with the lowest resistance. The most favorable results, showed a sheet resistance of approximately 100 $\frac{\Omega}{sq}$, indicating the material's good conductivity properties.

4.2.2 Optical properties

For examining optical properties, a robust characterization technique like ellipsometry can be employed. This effective method, which was previously introduced in the

"Methodology" section, allows for the characterization of various properties such as the refractive index, extinction coefficient, thickness, and others. This is achieved by analyzing the surface with an incident light beam. As mentioned earlier, it's crucial to have a physical model to compare the measurements with, in order to derive meaningful results. Creating a physical model that describes the material using harmonic oscillators is particularly challenging when dealing with an unexplored material. It's important to consider the material's chemical structure and corroborate the findings with other characterization techniques to ensure the validity of the results.

Fig. 4.3 Generic model parameters

To develop the model for PEDOT, I took into account the anisotropic nature of the material, which arises from its oriented polymeric chains. It's also essential to define the ε_∞ value, which adds a constant offset to all index values. This adjustment approximates the impact of absorption that happen far from the wavelengths we measured.

Another crucial aspect to consider are the poles. Poles are equivalent to Lorentz oscillators with zero broadening. They help describe the dispersion caused by absorptions that take place outside the spectral range that was measured.

$$\varepsilon_{pole_n} = \frac{Amp_n}{En_n^2 - E^2} \tag{4.2}$$

Where n is the oscillator number, while En_n (eV) and Amp_n (eV^2) are the energy and amplitude of the oscillator n.

The first oscillator used to describe the physic behaviour of the material is a Druide oscillator. The classic Drude model describes free carrier effects on the dielectric response. Its form is equivalent to a Lorentz oscillator with center energy equal to zero.

1: Type = Drude(RT) Resistivity (Ohm·cm)1 = 0.005600 (fit) Scat. Time (fs)1 = 1.008 (fit)
2: Type = Lorentz Amp2 = 10.000000 (fit) Br2 = 0.8735 (fit) En2 = 0.205 (fit)
3: Type = Lorentz Amp3 = 2.6919E-05 (fit) Br3 = 5.6380E-07 (fit) En3 = 6.5307E-08 (fit)
4: Type = Lorentz Amp4 = 11.392619 (fit) Br4 = 0.2649 (fit) En4 = 7.579 (fit)
5: Type = Lorentz Amp5 = 9.386850 (fit) Br5 = 0.7355 (fit) En5 = 0.204 (fit)
6: Type = Lorentz Amp6 = 4.856200 (fit) Br6 = 0.0070 (fit) En6 = 0.151 (fit)
7: Type = Lorentz Amp7 = 12.210000 (fit) Br7 = 0.0036 (fit) En7 = 0.148 (fit)
8: Type = Lorentz Amp8 = 8.150000 (fit) Br8 = 0.0020 (fit) En8 = 0.141 (fit)
9: Type = Lorentz Amp9 = 11.850000 (fit) Br9 = 0.0010 (fit) En9 = 0.135 (fit)
10: Type = Lorentz Amp10 = 12.370000 (fit) Br10 = 0.0020 (fit) En10 = 0.129 (fit)

Fig. 4.4 Drude and Lorentz oscillators parameters present in the model.

$$\varepsilon_{Drude(RT)}(E) = \frac{-\hbar^2}{\varepsilon_0 \rho_n (\tau_n E^2 + i\hbar E)} \tag{4.3}$$

Where n is the oscillator number, $\rho(\Omega cm)$ is the resistivity and $\tau(fs)$ the scattering time.

The other oscillators are Classic Lorentz oscillator model that describe optical response of bound charges.

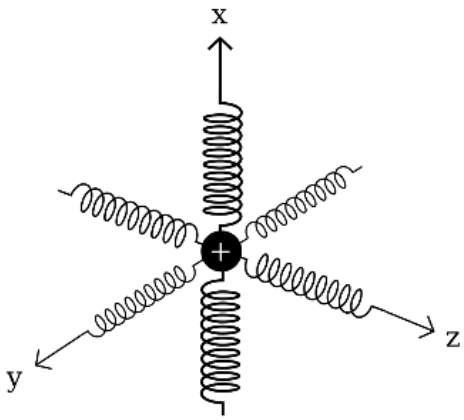

Fig. 4.5 Graphical representation of bounding forces between electrons and ions.

$$\varepsilon_{Lorentz} = \frac{Amp_n Br_n En_n}{En_n^2 - E^2 - iEBr_n} \tag{4.4}$$

Where n is the oscillator number, while $En_n(eV)$, $Br_n(eV)$, and Amp_n(no units) are the energy, broadening and amplitude of the oscillator n respectively.

Other parameters used to describe the material are the Euler angels. Euler angles determine the orientation of optical axes relative to the ellipsometer measurement

orientation. Optical axes are the directions where refractive index is considered constant, they occur only with anisotropic materials.

Since the material is measured on a support or substrate, the probing light interacts with it as well, carrying information about the substrate too. Therefore, it is necessary to describe the substrate and take it into account when analyzing the results. To physically represent the substrate, I used a Cauchy model, which is typically used to describe the refractive index and extinction coefficient of bulk materials.

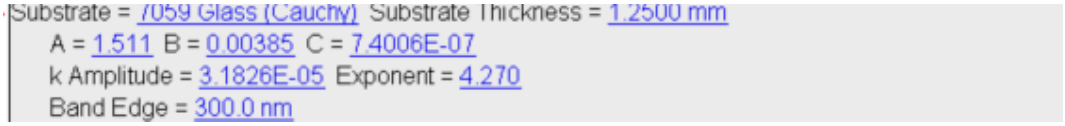

Fig. 4.6 Model parameters used to describe the substrate.

The Cauchy's equation for refractive index is the following:

$$n(\lambda) = A + \frac{B}{\lambda^2} + \frac{C}{\lambda^4} + ... \tag{4.5}$$

Where A is proportional to the density of free electrons and represents the Drude contribution. B is proportional the density of atoms and represents the dispersion effects due to the polarizability of the atoms. C is proportional to the density of phonons and represents the dispersion effects due to the polarizability of the phonons.

While extinction coefficient k is described by:

$$k = k_{Amp} e^{q(E - E_{bandgap})} \tag{4.6}$$

Where k_{Amp} and q are fit parameters for determining the shape of the extinction coefficient dispersion.

Finally it's possible to consider in the model the back-side reflections (Figure 4.7). Back-side reflections are undesirable when characterizing surface films. This is especially true if the substrate is anisotropic. If the backside reflections can't be avoided, the "incoherent" summation of light beams can be handled mathematically.

The accuracy of the fit demonstrates the correct functioning of the model used (Figure 4.8).

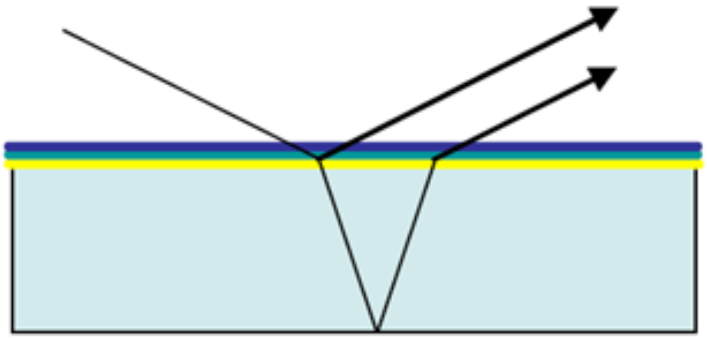

Fig. 4.7 Schematic representation of back-side reflections in multi-layer samples.

With the implemented model that captures the optical behavior of the material across a broad spectrum, it's possible to conduct measurements using ellipsometry. For these measurements, I utilized a J.A. Woollam RC2® Ellipsometer, which enables the creation of a 2D map of the surface (Figure 4.9). This device measures the optical properties at various points on the surface.

The refractive index of the material was found to be between 1.4 and 1.5. While this is not as high as with dielectric materials, it is still a commendable value considering the organic nature of PEDOT. Additionally, the extinction coefficient was found to be quite low, which indicates low losses in the visible range (Figure 4.10).

4.3 Organic nanostructures fabrication

Having gathered information on PEDOT from the measurements, we can now proceed with nanofabrication. The goal is to create an optical modulator using an interdigitated structure. This kind of modulator employs a unique design feature: interdigitated electrodes. These electrodes are arranged in a pattern resembling fingers, closely spaced and alternately interwoven. When an electric signal is applied to these electrodes, the resulting electric field changes the refractive index of the electro-optic material. This alteration in refractive index can modulate a light signal passing through the material. By adjusting the electric signal, we can control the optical properties of the light, such as its phase or intensity. These modulators are

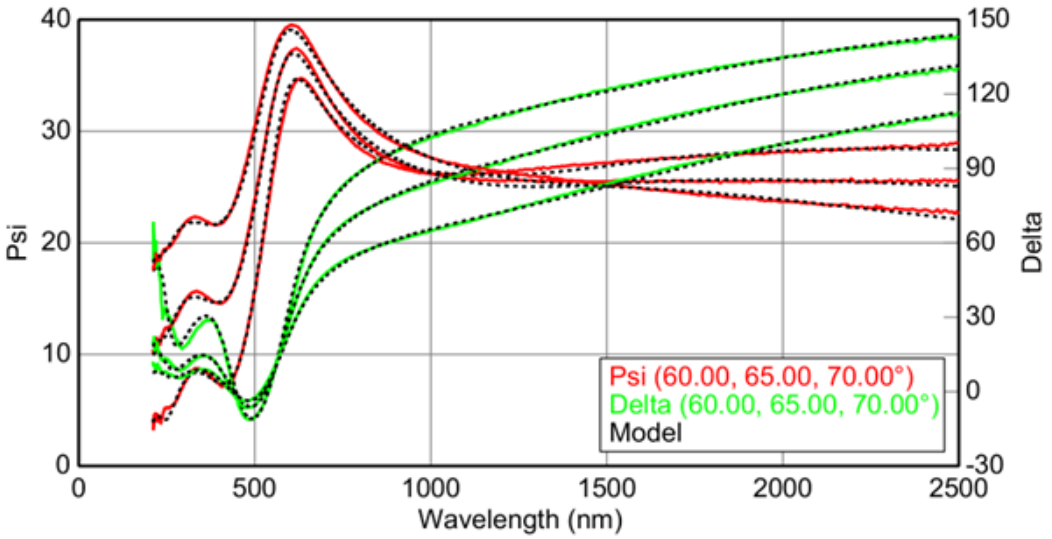

Fig. 4.8 Psi and Delta measurements of PEDOT film acquired with ellipsometer. The measured has been acquired with different incident angles (60°, 65°, and 70°C). The black dashed lines represent the same values theoretically predicted by the model.

extensively used in fiber-optic communications to encode information onto a light beam. They also have applications in other areas that require precise light control, like optical signal processing, sensors, and quantum computing.

Given the function of electrodes, they are typically made from conductive materials like gold. However, metallic materials exhibit very high losses in the visible range, significantly diminishing the device's performance by creating a shadow effect that reduces the signal's intensity. To address this issue, PEDOT can be utilized to create the electrodes. This is due to PEDOT's conductivity and, importantly, the optical properties we've measured indicate a substantial reduction in losses in the visible range.

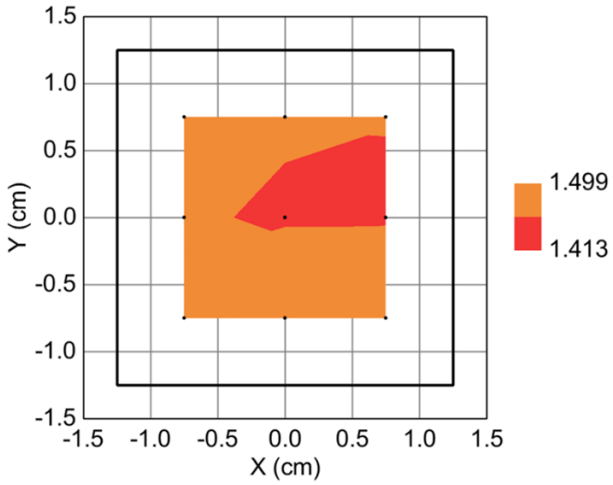

Fig. 4.9 Map of the distribution of the refractive index at the frequency of 632.8nm acquired with ellipsometer for a thin film of PEDOT on glass substrate.

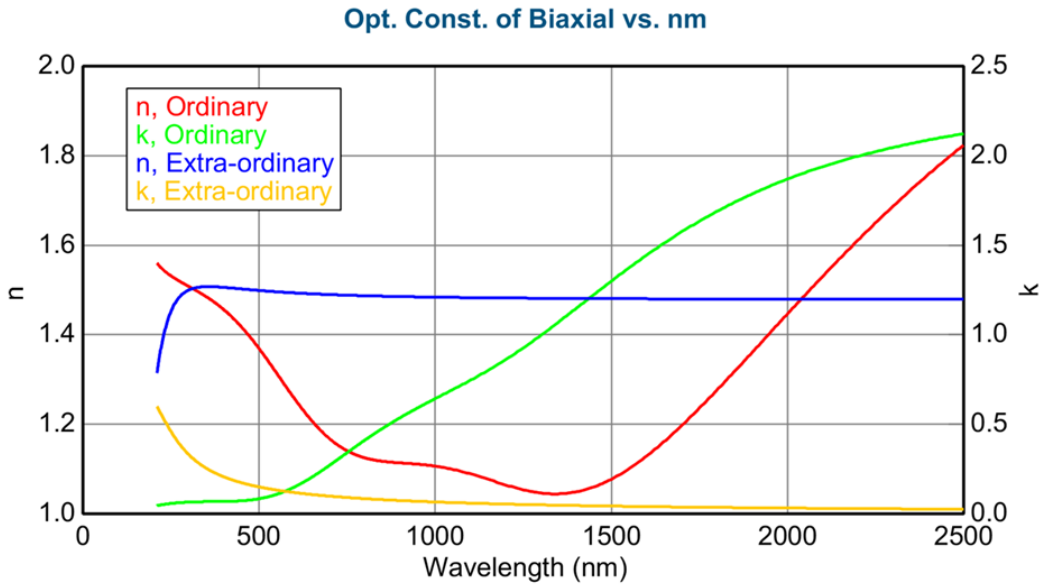

Fig. 4.10 Anisotropic optical constants of PEDOT film acquired with an ellipsometer in-plane and out-plane oriented.

4.3.1 Electronic resist on PEDOT

To determine the most effective approach for nanopatterning PEDOT, it's necessary to consider the sample's morphology. In this case, PEDOT is synthesized on a glass substrate. The synthesis technique, which involves acids, rules out the use of a PDMS mask. Therefore, EBL appears to be the most suitable technique. As outlined in the methodology, nanopatterning with EBL requires creating a mask with an electron-sensitive resist. Generally, this process involves baking the resist coating before exposure. Standard recipes provided by commercial resist manufacturers usually recommend baking temperatures around 180°C for 3-5 minutes. However, this temperature is not suitable for organic materials, especially PEDOT, which deteriorates at high temperatures, affecting its electrical conductivity performance.

To address this issue, I modified the standard recipes by lowering the baking temperature and extending the baking time to ensure the solvent in the resist mixture evaporates before exposure. If the temperature is too low, it hinders the complete evaporation of the solvent, leading to instability in the developed structures and causing deformation of the mask before etching. I found that 120°C is an acceptable temperature for evaporating the solvent without significantly impacting the properties of PEDOT. To compensate for the lower temperature, I increased the baking time to 15 minutes.

4.3.2 Electronic Beam Lithography on PEDOT

Having established the recipe for correctly coating the resist, the next step involves exposing the resist to the electron beam. A key aspect to consider here is the proximity effect. When electrons hit the surface, scattering occurs due to interaction with the material's atoms, which can deflect the electrons' trajectory. These scattered electrons can travel a certain distance in the resist, inadvertently exposing areas outside the intended target. While the energy transmitted to the resist by these scattered electrons is low compared to the main beam, the cumulative effect of exposure around a specific point can result in a significant dose, leading to unintended exposure of the resist.

To mitigate the proximity effect, it's necessary to appropriately regulate the exposure in areas with a high density of exposure points. This process is executed

using specific software that adjusts the dose distribution according to the patterning scheme and parameters dependent on the type of resist and substrate used (Figure 4.11).

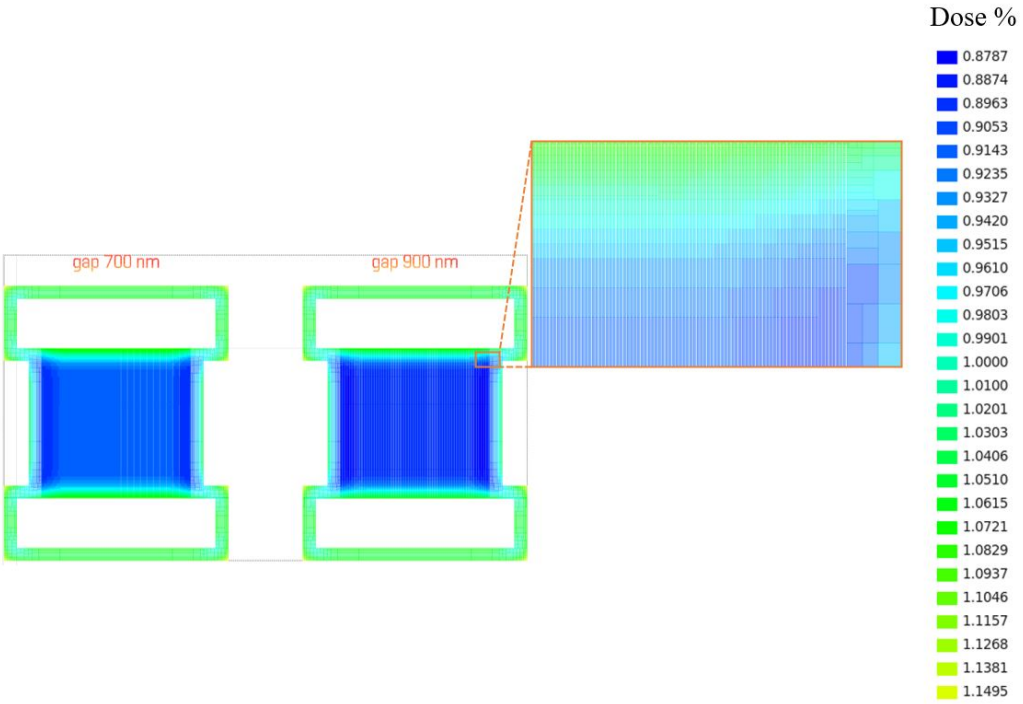

Fig. 4.11 Colored representation of the exposing dose distribution for electron beam lithography. Each color is associated with a different value of dose, from dark blue (lowest dose) to yellow (highest dose). Higher dense zone are exposed with lower dose to compensate the proximity effect.

4.3.3 PEDOT etching

After exposing the resist, we can proceed with etching the material beneath the mask. This aspect has already been explained in the methodology section, and here I will focus on the specific challenges related to etching organic materials such as PEDOT. The choice of gas mixture for etching depends on the chemical nature of the material. Since PEDOT is an organic material, oxygen is an excellent reactive gas for effectively and rapidly removing organic material.

A primary concern is that the resist materials are also organic, meaning that both the resist and PEDOT have the same etching rate, which limits the effectiveness of

the mask. This issue can be resolved by creating a mask that is three times thicker than the PEDOT layer to be etched. This approach is feasible in this case because the structure (constituting the interdigitated stripes) is thin and wide, allowing for a stable structure even when the thickness is tripled.

After etching, the remaining resist can be removed with acetone. PEDOT is insoluble and thus unaffected by solvents like acetone, making it safe to remove the resist. However, it's important to consider PEDOT's low adhesion to the glass substrate. This means mechanical removal methods, such as an ultrasonic bath, are not suitable due to the risk of dislodging the PEDOT.

The final results are shown with images acquired with optical microscope (Figure 4.12) and scanning electroN microscOpe (Figure 4.13).

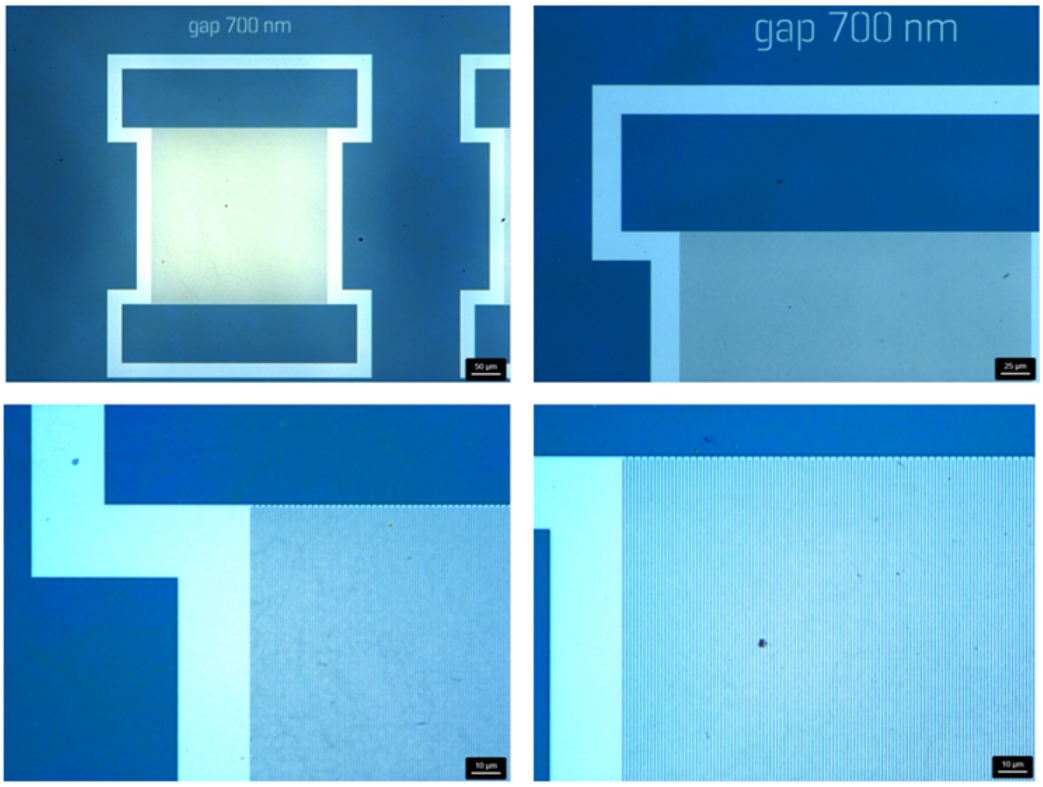

Fig. 4.12 Images of interdigitate structures in PEDOT acquired with optical microscope with different magnifications. The dark blue areas in PEDOT are surrounded by glass substrate where PEDOT has been removed.

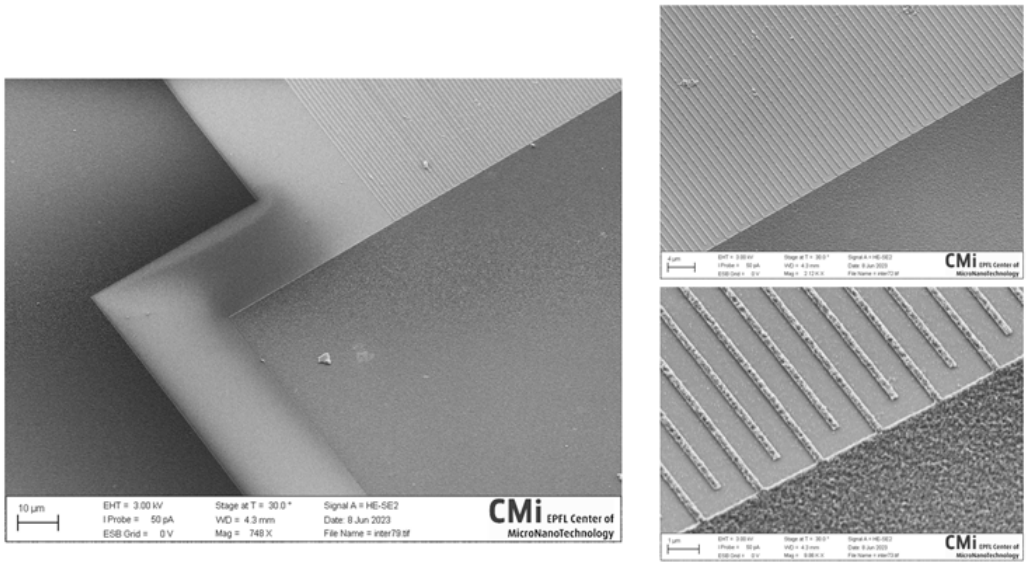

Fig. 4.13 Interdigitates structures in PEDOT acquired with scanning electron microscope.

Conclusion

Summary

To conclude this thesis, we want to summarize the key points presented in this work. The thesis presents a comprehensive study of metalenses, which are a class of metasurfaces offering innovative ways to manipulate light. These metalenses have potential applications in various fields, including optics and photonics.

Following, we delve into the design principles and fabrication techniques of these metalenses and metasurfaces. Special attention is given to the electron beam lithography and nanosphere lithography methods, highlighting the technical challenges and solutions in crafting these nanostructures.

Subsequently, the exploration of Fano resonances in photonic nanostructures forms a crucial part of our thesis. We demonstrate how the geometry of the pillars and the surrounding medium's refractive index can influence these resonances, which are critical in the field of nanophotonics.

A significant portion of our work focuses, then, on the use of organic materials, specifically PEDOT, in optical modulators. This section explores the advantageous properties of organic materials like low optical losses and moderate electrical conductivity, which are beneficial in light modulation applications. We conduct in-depth analyses of the optical properties of the structures we've created, using various characterization techniques like ellipsometry and profilometry. This includes studying the refractive index, extinction coefficient, and the overall behavior of these materials when interacting with light.

Limitations and future developments

Current nanofabrication techniques, while precise, may not be scalable for industrial production. High-resolution methods like Electron Beam Lithography are time-consuming and costly for large-scale applications. Expanding on fabrication scalability, future research could explore the development of hybrid or parallelized fabrication methods that enhance throughput without sacrificing the nanometric precision required for metasurface patterning. Techniques such as directed self-assembly (DSA) combined with nanoimprint lithography (NIL) could offer pathways to cost-effective, large-area production, enabling commercial viability for applications like display technologies and solar panels.

Moreover, metasurfaces might exhibit reduced efficiency in manipulating light across different wavelengths, especially in the infrared and ultraviolet spectrums. This could limit their application in broadband optical devices. Improving broadband efficiency necessitates a multidisciplinary approach, combining material science, electromagnetic theory, and computational optimization to design metasurfaces that maintain high performance across a wider spectrum. This could involve the use of multi-resonant structures that can operate efficiently at multiple wavelengths simultaneously or the development of new materials with meta-atoms that exhibit tunable responses to different light frequencies.

Additionally, the materials used in metasurface fabrication may not withstand prolonged exposure to harsh environmental conditions, affecting the long-term reliability of devices. Investigating materials with higher durability or developing protective coatings could extend the lifespan of metasurface-based devices, especially for outdoor applications. To enhance the environmental resilience of metasurfaces, research could focus on identifying or synthesizing materials that are inherently resistant to degradation from UV exposure, moisture, and temperature fluctuations. Additionally, the development of advanced protective coatings that do not impair the optical properties of metasurfaces could provide a means to extend device lifetimes in demanding environmental conditions.

Finally, future research could explore the integration of metasurfaces with electronic and photonic systems, opening up new functionalities in sensing, telecommunications, and computational imaging. This integration presents an opportunity to create compact, multifunctional devices. This could involve the co-design of meta-

surfaces with semiconductor lasers for enhanced light sources, integration with fiber optic systems for improved signal processing, or the development of metasurface-based sensors that can operate within electronic circuits for real-time environmental monitoring or health diagnostics.

Results and discussion

In my thesis I have systematically addressed gaps in current metasurface technologies by developing methods for new device design and utilizing cutting-edge fabrication techniques. This approach has significantly contributed to advancing the nanofabrication of metasurfaces. Through meticulous experimental and theoretical methods, including FEM simulations and EBL for fabrication, my work has provided valuable insights into the electromagnetic behavior of metasurfaces. This includes achieving precise control over light manipulation at the nanoscale, which is pivotal for the advancement of optical technologies.

My research not only tackles current technological challenges but also establishes the groundwork for future advancements by contributing to the development of more efficient, compact, and cost-effective photonic devices. This work has wide-ranging implications for various applications, including imaging, sensing, telecommunications, and more.

The findings of my thesis offer insights into metasurface technology, aiming to connect theoretical knowledge with practical applications. This contribution may support the field's innovation and its influence on future technological progress.

References

[1] D. R. Smith, Willie J. Padilla, D. C. Vier, S. C. Nemat-Nasser, and S. Schultz. Composite medium with simultaneously negative permeability and permittivity. *Phys. Rev. Lett.*, 84:4184–4187, 2000.

[2] J. B. Pendry. Negative refraction makes a perfect lens. *Phys. Rev. Lett.*, 85:3966–3969, 2000.

[3] Nanfang Yu, Patrice Genevet, Mikhail A. Kats, Francesco Aieta, Jean-Philippe Tetienne, Federico Capasso, and Zeno Gaburro. Light propagation with phase discontinuities: Generalized laws of reflection and refraction. *Science*, 334(6054):333–337, 2011.

[4] Alexander V. Kildishev, Alexandra Boltasseva, and Vladimir M. Shalaev. Planar photonics with metasurfaces. *Science*, 339(6125):1232009, 2013.

[5] Francesco Aieta, Patrice Genevet, Mikhail A. Kats, Nanfang Yu, Romain Blanchard, Zeno Gaburro, and Federico Capasso. Aberration-free ultrathin flat lenses and axicons at telecom wavelengths based on plasmonic metasurfaces. *Nano Letters*, 12(9):4932–4936, 2012.

[6] Yash D. Shah, Peter W. R. Connolly, James P. Grant, Danni Hao, Claudio Accarino, Ximing Ren, Mitchell Kenney, Valerio Annese, Kirsty G. Rew, Zoë M. Greener, Yoann Altmann, Daniele Faccio, Gerald S. Buller, and David R. S. Cumming. Ultralow-light-level color image reconstruction using high-efficiency plasmonic metasurface mosaic filters. *Optica*, 7(6):632–639, 2020.

[7] Aobo Li, Shreya Singh, and Dan Sievenpiper. Metasurfaces and their applications. *Nanophotonics*, 7(6):989–1011, 2018.

[8] Nasim Mohammadi Estakhri and Andrea Alù. Recent progress in gradient metasurfaces. *J. Opt. Soc. Am. B*, 33(2):A21–A30, 2016.

[9] Amir Arbabi, Yu Horie, Mahmood Bagheri, and Andrei Faraon. Dielectric metasurfaces for complete control of phase and polarization with subwavelength spatial resolution and high transmission. *Nature Nanotechnology*, 10(11):937–943, 2015.

[10] Guoxing Zheng, Holger Mühlenbernd, Mitchell Kenney, Guixin Li, Thomas Zentgraf, and Shuang Zhang. Metasurface holograms reaching 80% efficiency. *Nature Nanotechnology*, 10(4):308–312, 2015.

[11] Mohammadreza Khorasaninejad, Wei Ting Chen, Robert C. Devlin, Jaewon Oh, Alexander Y. Zhu, and Federico Capasso. Metalenses at visible wavelengths: Diffraction-limited focusing and subwavelength resolution imaging. *Science*, 352(6290):1190–1194, 2016.

[12] Francesco Aieta, Mikhail A. Kats, Patrice Genevet, and Federico Capasso. Multiwavelength achromatic metasurfaces by dispersive phase compensation. *Science*, 347(6228):1342–1345, 2015.

[13] Lingling Huang, Xianzhong Chen, Holger Mühlenbernd, Hao Zhang, Shumei Chen, Benfeng Bai, Qiaofeng Tan, Guofan Jin, Kok-Wai Cheah, Cheng-Wei Qiu, Jensen Li, Thomas Zentgraf, and Shuang Zhang. Three-dimensional optical holography using a plasmonic metasurface. *Nature communications*, 4:2808, 2013.

[14] Xingjie Ni, Alexander Kildishev, and Vladimir Shalaev. Metasurface holograms for visible light. *Nature communications*, 4:2807, 2013.

[15] Dianmin Lin, Pengyu Fan, Erez Hasman, and Mark Brongersma. Dielectric gradient metasurface optical elements. *Science (New York, N.Y.)*, 345:298–302, 2014.

[16] Anders Pors and Sergey I. Bozhevolnyi. Plasmonic metasurfaces for efficient phase control in reflection. *Opt. Express*, 21(22):27438–27451, 2013.

[17] Alexander E. Minovich, Andrey E. Miroshnichenko, Anton Y. Bykov, Tatiana V. Murzina, Dragomir N. Neshev, and Yuri S. Kivshar. Functional and nonlinear optical metasurfaces. *Laser & Photonics Reviews*, 9(2):195–213, 2015.

[18] Amir Arbabi, Ryan M. Briggs, Yu Horie, Mahmood Bagheri, and Andrei Faraon. Efficient dielectric metasurface collimating lenses for mid-infrared quantum cascade lasers. *Opt. Express*, 23(26):33310–33317, 2015.

[19] Costas M. Soukoulis, Stefan Linden, and Martin Wegener. Negative refractive index at optical wavelengths. *Science*, 315(5808):47–49, 2007.

[20] Mohammad Habib Ullah, Mohammad Tariqul Islam, and Mohammad Rashed Iqbal Faruque. A near-zero refractive index meta-surface structure for antenna performance improvement. *Materials*, 6(11):5058–5068, 2013.

[21] N. I. Landy, S. Sajuyigbe, J. J. Mock, D. R. Smith, and W. J. Padilla. Perfect metamaterial absorber. *Phys. Rev. Lett.*, 100:207402, 2008.

[22] Jacob Engelberg and Uriel Levy. The advantages of metalenses over diffractive lenses. *Nature Communications*, 11(1):1991, 2020.

[23] Moon Seong-Won Rho Junsuk Jeon Dongmin, Shin Kilsoo. Recent advancements of metalenses for functional imaging. *Nano Convergence*, 10(1):24, 2023.

[24] Metasurfaces go mainstream. *Nat. Photon.*, 17:022–01137–1, 2023.

[25] Saman Jahani and Zubin Jacob. All-dielectric metamaterials. *Nature Nanotechnology*, 11(1):23–36, 2016.

[26] Wei Ting Chen, Alexander Y. Zhu, Vyshakh Sanjeev, Mohammadreza Khorasaninejad, Zhujun Shi, Eric Lee, and Federico Capasso. A broadband achromatic metalens for focusing and imaging in the visible. *nature nanotechnology*, 13:220–226, 2018.

[27] Omid Hemmatyar, Sajjad Abdollahramezani, Yashar Kiarashinejad, Mohammadreza Zandehshahvar, and Ali Adibi. Full color generation with fano-type resonant hfo2 nanopillars designed by a deep-learning approach. *Nanoscale*, 11:21266–21274, 2019.

[28] Nishant Nookala, Jongwon Lee, Mykhailo Tymchenko, J. Sebastian Gomez-Diaz, Frederic Demmerle, Gerhard Boehm, Kueifu Lai, Gennady Shvets, Markus-Christian Amann, Andrea Alu, and Mikhail Belkin. Ultrathin gradient nonlinear metasurface with a giant nonlinear response. *Optica*, 3(3):283–288, 2016.

[29] Tomer Stav, Arkady Faerman, Elhanan Maguid, Dikla Oren, Vladimir Kleiner, Erez Hasman, and Mordechai Segev. Quantum entanglement of the spin and orbital angular momentum of photons using metamaterials. *Science*, 361(6407):1101–1104, 2018.

[30] Chuanlin Li, Peng Yu, Yongjun Huang, Qiang Zhou, Jiang Wu, Zhe Li, Xin Tong, Qiye Wen, Hao-Chung Kuo, and Zhiming M. Wang. Dielectric metasurfaces: From wavefront shaping to quantum platforms. *Progress in Surface Science*, 95(2):100584, 2020.

[31] Guixin Li, Shuang Zhang, and Thomas Zentgraf. Nonlinear photonic metasurfaces. *Nature Reviews Materials*, 2(5):17010, 2017.

[32] Isabelle Staude and Jörg Schilling. Metamaterial-inspired silicon nanophotonics. *Nature Photonics*, 11(5):274–284, 2017.

[33] Zhi-Bin Fan, Zeng-Kai Shao, Ming-Yuan Xie, Xiao-Ning Pang, Wen-Sheng Ruan, Fu-Li Zhao, Yu-Jie Chen, Si-Yuan Yu, and Jian-Wen Dong. Silicon nitride metalenses for close-to-one numerical aperture and wide-angle visible imaging. *Phys. Rev. Appl.*, 10:014005, 2018.

[34] Sajid M. Choudhury, Di Wang, Krishnakali Chaudhuri, Clayton DeVault, Alexander V. Kildishev, Alexandra Boltasseva, and Vladimir M. Shalaev. Material platforms for optical metasurfaces. *Nanophotonics*, 7(6):959–987, 2018.

[35] Mohammadreza Zandehshahvar, Yashar Kiarashinejad, Muliang Zhu, Hossein Maleki, Tyler Brown, and Ali Adibi. Manifold learning for knowledge discovery and intelligent inverse design of photonic nanostructures: Breaking the geometric complexity. *ACS Photonics*, 9(2):714–721, 2022.

[36] Ning An, Kaiyang Wang, Haohan Wei, and Qinghai Song. Fabricating high refractive index titanium dioxide film using electron beam evaporation for all-dielectric metasurfaces. *MRS Communications*, 6:77–83, 2016.

[37] Igor Aharonovich, Andrew D. Greentree, and Steven Prawer. Diamond photonics. *Nature Photonics*, 5(7):397–405, 2011.

[38] Igor Aharonovich, Dirk Englund, and Milos Toth. Solid-state single-photon emitters. *Nature Photonics*, 10(10):631–641, 2016.

[39] Jingyuan Linda Zhang, Konstantinos G. Lagoudakis, Yan-Kai Tzeng, Constantin Dory, Marina Radulaski, Yousif Kelaita, Kevin A. Fischer, Shuo Sun, Zhi-Xun Shen, Nicholas A. Melosh, Steven Chu, and Jelena Vučković. Complete coherent control of silicon vacancies in diamond nanopillars containing single defect centers. *Optica*, 4(11):1317–1321, 2017.

[40] Tamiko Masuda, Matthew Mitchell, Behzad Khanaliloo, David P. Lake, Thomas Lutz, JP E. Hadden, Wolfgang Tittel, and Paul E. Barclay. High-q diamond microdisks for coupling to siv quantum emitters. In *Conference on Lasers and Electro-Optics*, page JTh3E.2. Optica Publishing Group, 2017.

[41] Prasoon K. Shandilya, Sigurd Flågan, Natalia C. Carvalho, Elham Zohari, Vinaya K. Kavatamane, Joseph E. Losby, and Paul E. Barclay. Diamond integrated quantum nanophotonics: Spins, photons and phonons. *Journal of Lightwave Technology*, 40(23):7538–7571, 2022.

[42] Tzu-Yung Huang, Richard R. Grote, Sander A. Mann, David A. Hopper, Annemarie L. Exarhos, Gerald G. Lopez, Amelia R. Klein, Erik C. Garnett, and Lee C. Bassett. A monolithic immersion metalens for imaging solid-state quantum emitters. *Nature Communications*, 10(1):2392, 2019.

[43] Jixiang Jing, Yau Chuen Yiu, Cong Chen, Dangyuan Lei, Lei Shao, Qi Wang, Kwai Hei Li, Ngai Wong, and Zhiqin Chu. A data-mining-assisted design of structural colors on diamond metasurfaces. *Advanced Photonics Research*, 3(3):2100292, 2022.

[44] Qixin Shen, Amirhassan Shams-Ansari, Andrew M. Boyce, Nathaniel C. Wilson, Tao Cai, Marko Loncar, and Maiken H. Mikkelsen. A metasurface-based diamond frequency converter using plasmonic nanogap resonators. *Nanophotonics*, 10(1):589–595, 2021.

[45] Soumen Mandal. Nucleation of diamond films on heterogeneous substrates: a review. *RSC Adv.*, 11:10159–10182, 2021.

[46] Oliver A. Williams, Olivier Douhéret, Michael Daenen, Ken Haenen, Eiji Ōsawa, and Makoto Takahashi. Enhanced diamond nucleation on monodispersed nanocrystalline diamond. *Chemical Physics Letters*, 445(4):255–258, 2007.

[47] S. Yugo, T. Kanai, T. Kimura, and T. Muto. Generation of diamond nuclei by electric field in plasma chemical vapor deposition. *Applied Physics Letters*, 58(10):1036–1038, 1991.

[48] Daniil M. Lukin, Constantin Dory, Melissa A. Guidry, Ki Youl Yang, Sattwik Deb Mishra, Rahul Trivedi, Marina Radulaski, Shuo Sun, Dries Vercruysse, Geun Ho Ahn, and Jelena Vučković. 4h-silicon-carbide-on-insulator for integrated quantum and nonlinear photonics. *Nature Photonics*, 14(5):330–334, 2020.

[49] Son Tung Ha, Yuan Hsing Fu, Naresh Kumar Emani, Zhenying Pan, Reuben M. Bakker, Ramón Paniagua-Domínguez, and Arseniy I. Kuznetsov. Directional lasing in resonant semiconductor nanoantenna arrays. *Nature Nanotechnology*, 13:1748–3395, 2018.

[50] Christian Kramer, Martin Schäferling, Thomas Weiss, Harald Giessen, and Tobias Brixner. Analytic optimization of near-field optical chirality enhancement. *ACS Photonics*, 4(2):396–406, 2017.

[51] Chengcong Cui, Chaobiao Zhou, Shuai Yuan, Xingzhi Qiu, Liangqiu Zhu, Yuxi Wang, Yi Li, Jinwen Song, Qingzhong Huang, Yi Wang, Cheng Zeng, and Jinsong Xia. Multiple fano resonances in symmetry-breaking silicon metasurface for manipulating light emission. *ACS Photonics*, 5(10):4074–4080, 2018.

[52] Zhuojun Liu, Yi Xu, Ye Lin, Jin Xiang, Tianhua Feng, Qitao Cao, Juntao Li, Sheng Lan, and Jin Liu. High-q quasibound states in the continuum for nonlinear metasurfaces. *Phys. Rev. Lett.*, 123:253901, 2019.

[53] H. R. Phillip and E. A. Taft. Kramers-kronig analysis of reflectance data for diamond. *Phys. Rev.*, 136:A1445–A1448, 1964.

[54] Boris Luk'yanchuk, Nikolay I. Zheludev, Stefan A. Maier, Naomi J. Halas, Peter Nordlander, Harald Giessen, and Chong Tow Chong. The fano resonance in plasmonic nanostructures and metamaterials. *Nature Materials*, 9:707–715, 2010.

[55] R. Alaee, R. Filter, D. Lehr, F. Lederer, and C. Rockstuhl. A generalized kerker condition for highly directive nanoantennas. *Opt. Lett.*, 40(11):2645–2648, 2015.

[56] Wei Liu and Yuri S. Kivshar. Generalized kerker effects in nanophotonics and meta-optics [invited]. *Opt. Express*, 26(10):13085–13105, 2018.

[57] Ronghui Lin, Zahrah Alnakhli, Feras AlQatari, and Xiaohang Li. Analysis of tapered nanopillars for reflective metalens: The role of higher-order modes. *IEEE Photonics Journal*, 12(4):1–7, 2020.

[58] Mikhail F. Limonov, Mikhail V. Rybin, Alexander N. Poddubny, and Yuri S. Kivshar. Fano resonances in photonics. *Nature Photonics*, 11:543–554, 2017.

[59] Xueer Chen, Yong Zhang, Guoxiong Cai, Jianliang Zhuo, Kunzhong Lai, and Longfang Ye. All-dielectric metasurfaces with high q-factor fano resonances enabling multi-scenario sensing. *Nanophotonics*, 11(20):4537–4549, 2022.

[60] Saman Jahani and Zubin Jacob. All-dielectric metamaterials. *Nat. Nanotechnol.*, 11(1):23–36, 2016.

[61] Mohammadreza Khorasaninejad and Federico Capasso. Metalenses: Versatile multifunctional photonic components. *Science*, 358(6367):eaam8100, 2017.

[62] Nishant Nookala, Jongwon Lee, Mykhailo Tymchenko, J. Sebastian Gomez-Diaz, Frederic Demmerle, Gerhard Boehm, Kueifu Lai, Gennady Shvets, Markus-Christian Amann, Andrea Alu, and Mikhail Belkin. Ultrathin gradient nonlinear metasurface with a giant nonlinear response. *Optica*, 3(3):283, 2016.

[63] Zhuojun Liu, Yi Xu, Ye Lin, Jin Xiang, Tianhua Feng, Qitao Cao, Juntao Li, Sheng Lan, and Jin Liu. High-q quasibound states in the continuum for nonlinear metasurfaces. *Phys. Rev. Lett.*, 123(253901), 2019.

[64] David Hähnel, Christian Golla, Maximilian Albert, Thomas Zentgraf, Viktor Myroshnychenko, Jens Förstner, and Cedrik Meier. A multi-mode super-fano mechanism for enhanced third harmonic generation in silicon metasurfaces. *Light: Sci. App.*, 12(1):2047–7538, 2023.

[65] Alexei V. Prokhorov, Mikhail Yu. Gubin, Alexander V. Shesterikov, Aleksey V. Arsenin, Valentyn S. Volkov, and Andrey B. Evlyukhin. Lasing effect in symmetrical van der waals heterostructured metasurfaces due to lattice-induced multipole coupling. *Nano Letters*, 2023.

[66] Omid Hemmatyar, Sajjad Abdollahramezani, Yashar Kiarashinejad, Mohammadreza Zandehshahvar, and Ali Adibi. Full color generation with fano-type resonant hfo2 nanopillars designed by a deep-learning approach. *Nanoscale*, 11:21266, 2019.

[67] Hatice Altug, Sang-Hyun Oh, Stefan A. Maier, and Jiří Homola. Advances and applications of nanophotonic biosensors. *Nat. Nanotechnol.*, 17(1):5–16, 2022.

[68] Huawei Chen, Xinye Fan, Wenjing Fang, Bingyuan Zhang, Shuangshuang Cao, Qinghe Sun, Dandan Wang, Huijuan Niu, Chuanchuan Li, Xin Wei, Chenglin Bai, and Santosh Kumar. High-q fano resonances in all-dielectric metastructures for enhanced optical biosensing applications. *Biomed. Opt. Express*, 15(1):294–305, 2024.

[69] Hening Zhao, Xinye Fan, Xin Wei, ChuanChuan Li, Tonggang Zhao, Wenjing Fang, Huijuan Niu, Chenglin Bai, and Santosh Kumar. Highly sensitive multiple fano resonances excitation on all-dielectric metastructure. *Opt. Rev.*, 30(2):208 – 216, 2023.

[70] Ileana-Cristina Benea-Chelmus, Sydney Mason, Maryna L. Meretska, Delwin L. Elder, Dmitry Kazakov, Amirhassan Shams-Ansari, Larry R. Dalton, and Federico Capasso. Gigahertz free-space electro-optic modulators based on mie resonances. *Nat. Commun.*, 13(1):3170, 2022.

[71] Kai Wang, James G. Titchener, Sergey S. Kruk, Lei Xu, Hung-Pin Chung, Matthew Parry, Ivan I. Kravchenko, Yen-Hung Chen, Alexander S. Solntsev, Yuri S. Kivshar, Dragomir N. Neshev, and Andrey A. Sukhorukov. Quantum metasurface for multiphoton interference and state reconstruction. *Science*, 361(6407):1104–1108, 2018.

[72] Yash D. Shah, Adetunmise C. Dada, James P. Grant, David R. S. Cumming, Charles Altuzarra, Thomas S. Nowack, Ashley Lyons, Matteo Clerici, and Daniele Faccio. An all-dielectric metasurface polarimeter. *ACS Photonics*, 9(3245-3252), 2022.

[73] Zhiwei Zheng, Ying Zhu, Junyi Duan, Meibao Qin, Feng Wu, and Shuyuan Xiao. Enhancing goos-hänchen shift based on magnetic dipole quasi-bound states in the continuum in all-dielectric metasurfaces. *Optics Express*, 29(18):29541–29549, 2021.

[74] Federico Capasso. Metaoptics for the consumer market. *Nature Photonics*, 17:6–7, 2023.

[75] M. Pourmand and Pankaj K. Choudhury. Light-matter interaction at the subwavelength scale: Pathways to design nanophotonic devices. *Adventures in Contemporary Electromagnetic Theory*, pages 281–314, 2023.

[76] Pavel Cheben, Robert Halir, Jens H. Schmid, Harry A. Atwater, and David R. Smith. Subwavelength integrated photonics. *Nature*, 560:565–570, 2018.

[77] Iman Sajedian, Heon Lee, and Junsuk Rho. Double-deep q-learning to increase the efficiency of metasurface holograms. *Scientific Reports*, 9:10899, 2019.

[78] Qian Ma, Che Liu, Qiang Xiao, Ze Gua, Xinxin Gao, Lianlin Li, and Tie Jun Cui. Information metasurfaces and intelligent metasurfaces. *Photonics Insights*, 1(1), 2022.

[79] Itzik Malkiel, Michael Mrejen, Achiya Nagler, Uri Arieli, Lior Wolf, and Haim Suchowski. Plasmonic nanostructure design and characterization via deep learning. *Light: Science & Applications*, 7(60), 2018.

[80] Junhwa Seong, Youngsun Jeon, Younghwan Yang, Trevon Badloe, and Junsuk Rho. Cost-effective and environmentally friendly mass manufacturing of optical metasurfaces towards practical applications and commercialization. *Int. J. Precis. Eng. Manuf. - Green Technol.*, 11(2), 2023.

[81] Nasim Mohammadi Estakhri, Brian Edwards, and Nader Engheta. Inverse-designed metastructures that solve equations. *Science*, 363(6433):1333–1338, 2019.

[82] David Pile. Metamaterials for the masses. *Nature Photonics*, 17:2–3, 2023.

[83] M. Kerker, D.-S. Wang, and C. L. Giles. Electromagnetic scattering by magnetic spheres. *J. Opt. Soc. Am.*, 73(6):765–767, 1983.

[84] Adrià Canós Valero, Hadi K. Shamkhi, Anton S. Kupriianov, Thomas Weiss, Alexander A. Pavlov, Dmitrii Redka, Vjaceslavs Bobrovs, Yuri Kivshar, and Alexander S. Shalin. Superscattering emerging from the physics of bound states in the continuum. *Nat. Commun.*, 14:4689, 2023.

[85] R. Alaee, R. Filter, D. Lehr, F. Lederer, and C. Rockstuhl. A generalized kerker condition for highly directive nanoantennas. *Optics Letters*, 40(11):2645, 2015.

[86] Zhenghe Zhang, Pengbo Liu, Wanli Lu, Ping Bai, Bingchang Zhang, Zefeng Chen, Stefan A. Maier, Jaime Gómez Rivas, Shaojun Wang, and Xiaofeng Li. High-q collective mie resonances in monocrystalline silicon nanoantenna arrays for the visible light. *Fundamental Research*, 3(5):822–830, 2023.

[87] Eleonora Cara, Federico Ferrarese Lupi, Matteo Fretto, Natascia De Leo, Mauro Tortello, Renato Gonnelli, Katia Sparnacci, and Luca Boarino. Directed self-assembly of polystyrene nanospheres by direct laser-writing lithography. *Nanomaterials*, 10(280), 2020.

[88] Magnus P. Jonsson, Andreas B. Dahlin, Peter Jönsson, and Fredrik Höök. Nanoplasmonic biosensing with focus on short-range ordered nanoholes in thin metal films. *Biointerphases*, 3:FD30–FD40, 2008.

[89] Irdi Murataj, Marwan Channab, Eleonora Cara, Candido F. Pirri, Luca Boarino, Angelo Angelini, and Federico Ferrarese Lupi. Hyperbolic metamaterials via hierarchical block copolymer nanostructures. *Adv. Opt. Materials*, 9(2001933), 2021.

[90] Changhang Huang, Yanyan Zhu, and Xingkun Man. Block copolymer thin films. *Physics Reports*, 932:1–36, 2021.

[91] Geon Gug Yang, Hee Jae Choi, Kyu Hyo Han, Jang Hwan Kim, Chan Woo Lee, Edwin Ino Jung, Hyeong Min Jin, and Sang Ouk Kim. Block copolymer nanopatterning for nonsemiconductor device applications. *ACS Appl. Mater. Interfaces*, 14(10):12011–12037, 2022.

[92] Nicholas J. Greybush, Victor Pacheco-Peña, Nader Engheta, Christopher B. Murray, and Cherie R. Kagan. Plasmonic optical and chiroptical response of self-assembled au nanorod equilateral trimers. *ACS Nano*, 13(2):1617–1624, 2019.

[93] Inc. SCHOTT North America. Optical glass data sheets.

[94] Vittorio Bonino and Angelo Angelini. High-q fano resonances in diamond nanopillars. *Opt. Mater. Express*, 13(4):1110, 2023.

[95] Mikhail F. Limonov, Mikhail V. Rybin, Alexander N. Poddubny, and Yuri S. Kivshar. Fano resonances in photonics. *Nature Photonics*, 11, 2017.

[96] Marco Riccardi, Andrei Kiselev, Karim Achouri, and Olivier J. F. Martin. Multipolar expansions for scattering and optical force calculations beyond the long wavelength approximation. *Physical Review B*, 106:115428, 2022.

[97] P. Grahn, A. Shevchenko, and M. Kaivola. Electromagnetic multipole theory for optical nanomaterials. *New J. Phys.*, 14:093033, 2012.

[98] Stefan Mühlig, Christoph Menzel, Carsten Rockstuhl, and Falk Lederer. Multipole analysis of meta-atoms. *Metamaterials*, 5:64–73, 2011.

End of the document